Residual flexural properties of CFRP sandwich structures with aluminum honeycomb cores after low-velocity impact

Wentao He , Shaojia Lu , Ke Yi , Shuqing Wang , Guangyong Sun , Zhiqiang Hu

PII: S0020-7403(19)30559-4
DOI: https://doi.org/10.1016/j.ijmecsci.2019.105026
Article Number: 105026
Reference: MS 105026

To appear in: *International Journal of Mechanical Sciences*

Received date: 16 February 2019
Revised date: 27 June 2019
Accepted date: 15 July 2019

Please cite this article as: Wentao He , Shaojia Lu , Ke Yi , Shuqing Wang , Guangyong Sun , Zhiqiang Hu , Residual flexural properties of CFRP sandwich structures with aluminum honeycomb cores after low-velocity impact, *International Journal of Mechanical Sciences* (2019), doi: https://doi.org/10.1016/j.ijmecsci.2019.105026

Highlights

- Low-velocity impact and residual flexural behaviors of honeycomb panels with different structural configurations are investigated.
- Core height has little effect on low-velocity behavior, but affects residual flexural strength significantly.
- Residual flexural strength almost reduces 20%-30% even through superficial impact damage remains barely visible.
- Bending failure pattern is related to core stiffness, but independent of the extent of impact-induced damage.
- Predicted impact load, absorbed energy, residual flexural strength and failure modes match well with experimental ones.

Residual flexural properties of CFRP sandwich structures with aluminum honeycomb cores after low-velocity impact

Wentao He[a,b*], Shaojia Lu[a,b], Ke Yi[c], Shuqing Wang[a,b*], Guangyong Sun[d], Zhiqiang Hu[e]

[a] College of Engineering, Ocean University of China, Qingdao 266100, China

[b] Shandong Provincial Key Laboratory of Ocean Engineering, Ocean University of China, Qingdao 266100, China

[c] CRRC Zhuzhou Locomotive Co., Ltd., Zhuzhou, 412001, China

[d] School of Aerospace, Mechanical and Mechatronic Engineering, The University of Sydney, Sydney, NSW 2006, Australia

[e] School of Engineering, Newcastle University, Newcastle Upon Tyne, NE1 7RU,UK

*Corresponding Author

E-mail: hewentao@ouc.edu.cn

Tel.: 86-532-66781550

Fax: 86-532-66781550

ABSTRACT

This paper aims to evaluate the influences of impact-induced damage on the residual flexural strength of honeycomb core sandwich panels with different structural configurations by combining the experimental, numerical and theoretical methods. Low-velocity impact tests and three-point bending tests after impact are carried out to determine and quantify the effects of structural configuration and impact energy on the impact damage and residual flexural strength of such structures. Subsequently, an integrated FE model with the VUMAT subroutine is developed to further investigate the damage states and failure mechanisms for the impact and bending simulation. The numerical results match well with the experimental ones in terms of impact load, absorbed energy, residual flexural strength and failure mechanisms. Results indicate that increasing cell wall thickness or decreasing side length of honeycomb core has significant effects on peak load, while increasing core height has little effect. Specimens with lower core stiffness fail through core buckling and crushing under the bending load, while specimen with higher core stiffness fails by top face sheet fracture. The residual flexural strength reduces markedly even through the impact damage is barely visible, indicating that it has a strong correlation with impact energy and structural configuration of cores.

Keywords: Honeycomb core sandwich structure; Impact response; Residual strength; Flexural behavior; Failure mode.

1. Introduction

Lightweight composites have been widely used to meet the ever-growing requirements of marine applications primarily due to their higher specific strength and stiffness as compared to metallic alloys [1-3]. Among the most promising composite structures, honeycomb core sandwich structures have been used as components of ship structural bulkheads, decks and superstructure where weight saving is a critical consideration [4-7]. However, despite excellent in-plane properties of composite structures, they are susceptible to damage from accidental low-velocity impact events occurring during assembly, maintenance and service [8-11]. Moreover, even barely visible damage severely diminishes the load-carrying capacity of composite components, possibly causing catastrophic failure of the integral structure during service life. For this reason, it is very necessary to provide insight into the low-velocity impact damage characterization and failure mechanisms of post-impacted composite sandwich structures before widely applied in the marine industry [12-15].

Residual compressive strength [16], residual tensile strength [17] and residual flexural strength after impact [18] are commonly used to evaluate and quantify the damage tolerance of the post-impacted composite components. From the previous review, considerable experimental and computational research studies have been conducted to determinate and predict the residual compressive strength of post-impacted composite structures, while few have been done on their residual tensile strength and residual flexural strength after impact [19]. The research literatures on the impact response and Compression-After-Impact (CAI) strength evaluation are focused on composite laminates, and their research emphasis can be summarized as: the failure mechanisms during impact, the relationship between residual strength and impact-induced damage, and the influences of structural parameters and material compositions on residual mechanical properties. It can be concluded from these studies that structural parameters and impact variables, such

as material compositions, stacking sequence, impact energy, impactor shape, impact location and boundary conditions, have different influences on residual properties after impact [20-22]. With respect to sandwich structures, a number of experimental and numerical studies have been conducted to investigate the influences of face-sheet/core thickness and their material types on the CAI strength and relevant failure mechanisms under various impact loading [23]. Key findings from these studies reveal that the residual compressive strength is closely related to the impact-induced damage of sandwich panels, such as matrix cracking, delamination and fiber fracture of the face sheet as well as the buckling and collapse of core. The residual compressive strength could be reduced up to 50% even through the superficial damage remains invisible [24]. Traditionally, the CAI strength has been widely used to evaluate the post-impact performance of composite components, since it was found that compression after impact could cause considerable reduction in structural integrity. However, recently many researchers have criticized the sole use of CAI to evaluate and quantify the residual load-carrying capacity, particularly for composite components mainly suffering from tensile and bending load.

Compared with residual compressive strength, impact damage has relatively little effect on the residual tensile strength, particularly for the low impact energy cases [25]. The primary failure modes at the low impact energy are delamination and matrix cracking, which are not very sensitive to the residual tensile strength. Most studies on the residual tensile properties are mainly for composite laminates, whereas the works on the residual tensile strength of sandwich structures remain to be rare to date [26-29]. Caprino and Teti [30] investigated the residual tensile strength of post-impact foam core sandwich structures with glass fiber face sheets. Wang et al. [31] obtained the relation curve of residual tensile strength against the impact energy of carbon fiber composite lattice core

sandwich structures, and the curve can be divided to three distinct stages according to the various impact energy levels.

The studies on the residual flexural properties are much less common than the residual compressive properties but have aroused increasingly more attention, particularly for the composite beam components subjected to bending load [32-36]. Many structural components in ship hull primarily undergo bending moments under wave action and therefore, it is essential to evaluate the residual flexural behaviors after impact for critical parts. The studies concerning the residual flexural behaviors are primarily performed experimentally, and their research emphasis can be summarized as: impact response in terms of impact load and energy absorption during the impact event, residual flexural properties after impact, failure modes and failure mechanisms during the whole process. Additionally, hybridization of composite laminates could improve the impact resistance and maintain satisfactory residual flexural strength, thus it highlights the positive role of the stacking sequence [35-37]. A comparison has been made between the residual flexural strength and compressive strength of 2D and 3D woven fiber-reinforced composites [38]. Key finding revealed that the former decreased significantly compared with the latter, indicating that the residual flexural properties were of crucial importance to provide impact resistance for structures. More particularly, there have been limited studies available to explore the residual flexural strength and failure mechanisms of sandwich structures [39, 40]. Klaus et al. [39] investigated the impact response and residual flexural behavior of aramid paper foldcore sandwich structures with CFRP face sheets. In the previous study, the authors in this paper investigated the residual flexural strength of composite sandwich structure with corrugated core by experimental and numerical methods [40]. It was found that the residual flexural strength decreased significantly, even for the damage at lower impact energy. However, to the author's knowledge, there have been fewer studies concerning the flexural behaviors of aluminum

honeycomb core sandwich structures with CFRP/GFRP face sheets [41, 42], but a study on the residual flexural strength after impact of such structures has not yet been reported.

This paper aims to investigate the impact-induced damage and residual flexural strength of honeycomb sandwich panels. Low-velocity impact tests are conducted to investigate the impact response characteristics of such structures considering different core configurations and various impact energy levels; three-point bending tests after impact are carried out to explore the influence of impact-induced damage on the residual flexural behavior of such structures. Then, an integrated FE model with the VUMAT subroutine in ABAQUS/Explicit is developed to further investigate the damage states and failure mechanisms for the impact and bending. Finally, the predicted and experimental results of impact response and flexural behavior are analyzed in detail.

2. Materials and specimens

In this paper, sandwich beams are constructed from thin-walled carbon fiber-reinforced polymer (CFRP) face sheets and aluminum hexagonal cells honeycomb cores with various geometry configurations, as illustrated in Fig. 1. The hexagonal honeycomb cores are made of AA3003 aluminum alloy foil (Fig. 1(b)), whose material properties are summarized in Table 1. To better explore the relationship between impact damage state and residual flexural strength, four kinds of sandwich panels with different structural configurations such as cell wall thickness, side length and core height are tested, and their structural parameters are listed in Table 2.

CFRP laminate is made from eight-layer unidirectional T700 carbon/epoxy prepreg (0.125 mm thickness) with stacking sequence 0°/90° by using compression molding technique. The properties of unidirectional carbon fiber provided by the manufacturer are given in Table 3. Both face sheets and a core are bonded together with epoxy adhesive film with 0.2 mm thickness under pressure of 0.5 MPa for 120 min by using hot pressing

machine. And then, the sandwich panels are cut into several specimens in 100 mm × 300 mm dimensions.

3. Experimental methodology

3.1 Impact tests

The impact response is evaluated by an instrumented drop weight impact testing machine in accordance with ASTM D7136 standard (2015) [43], as displayed in Fig. 2. A pneumatic-controlled anti-rebound system is installed on the testing equipment to avoid multi-hits. During impact event, the sandwich beam is clamped by a pneumatic fixture with a pair of steel panels, providing a central region of 75 mm diameter to be impacted. The pneumatic fixture provides an appropriate uniform pressure of 0.02 MPa to prevent the specimen from sliding and vibrating.

The drop weight with a hemispherical tip of 12 mm diameter weights 13.2 kg and is adopted to impact the center of specimens. Three typical impact energy levels, ranging from 5 J to 40 J, are employed to generate different degrees of damage for the sandwich beam. The initial impact energy can be transferred by potential energy of drop-weight. A piezoelectric transducer of 10 kN is adopted to record the history of impact load during the impact process by using a digital data acquisition system.

3.2 Three-point bending tests

The residual flexural behaviors of the post-impact sandwich beams are assessed by the three-point bending test using an electronic universal tester with a maximum loading capacity of 100 kN in accordance with ASTM D 790 [44]. The schematic diagram of experimental setup is illustrated in Fig. 3. The specimen is supported by two cylindrical rollers with a diameter of 30 mm and the support span distance is 200 mm. The specimen is loaded by a cylindrical indenter with a diameter of 30 mm. A constant feed rate of 2 mm/min is performed for the whole bending process. The load is applied on the impacted side of post-impact sandwich beam in order to explore the evolution process of the

delamination and fracture for the impacted face sheet under compressive stress. Additionally, the flexural properties of non-impacted specimen of each group are also evaluated to provide a baseline reference for identifying the sensitive design variables and quantifying the residual flexural strength.

4. Numerical simulation

4.1 Damage model for the aluminium core

Several damage initiation criteria built-in ABAQUS can be used to predict the onset of failure of ductile metals, including ductile and shear criteria, which associate with different kinds of material failure. In this study, the ductile damage criteria are employed to predict the progressive damage and failure of thin-walled metal sheet due to the nucleation, growth, and coalescence of voids. Damage initiates when the damage state ω_D is met:

$$\omega_D = \int \frac{\mathrm{d}\bar{\varepsilon}^{pl}}{\bar{\varepsilon}_D^{pl}(\eta, \dot{\bar{\varepsilon}}^{pl})} = 1 \tag{1}$$

where the equivalent plastic strain $\bar{\varepsilon}_D^{pl}$ is a function of stress triaxiality η and strain rate $\dot{\bar{\varepsilon}}^{pl}$. Once failure initiation is satisfied, the material stiffness is degraded during the damage process according to the energy-based evolution law. The exponential damage evolution law is employed for exponential softening of the stress-strain response for the aluminum alloy in this study.

4.2 Damage model for the composite face sheets

Composite laminates could experience intra-laminar and inter-laminar damage under impact loading. Several failure criteria have been formulated and implemented to predict the mechanical damage behaviors of composites, including Tsai-Wu [45], Hashin [46], Hou [47] and others [48]. Among them, Hashin failure criteria have been proved effective to characterize the composite damage, and are applied extensively due to their

brief expressions. In this paper, a progressive failure model including 3D Hashin and Yeh delamination failure criteria is expressed in the manner of strain component due to its relatively good continuity in comparison with stress [49]. The initiation criteria can be written as,

Fiber tensile failure:

$$R_{ft}^2 = \left(\frac{\varepsilon_{11}}{X_T^{\varepsilon}}\right)^2 + \left(\frac{\varepsilon_{12}}{S_{12}^{\varepsilon}}\right)^2 + \left(\frac{\varepsilon_{13}}{S_{13}^{\varepsilon}}\right)^2 \quad \varepsilon_{11} \geq 0 \tag{2}$$

Fiber compressive failure:

$$R_{fc}^2 = \left(\frac{\varepsilon_{11}}{X_C^{\varepsilon}}\right)^2 \quad \varepsilon_{11} \leq 0 \tag{3}$$

Matrix tensile failure:

$$R_{mt}^2 = \left(\frac{\varepsilon_{22}+\varepsilon_{33}}{Y_T^{\varepsilon}}\right)^2 + \left(\frac{1}{S_{23}^{\varepsilon}}\right)^2\left(\varepsilon_{23}^2 - \frac{E_{22}E_{33}}{G_{23}^2}\varepsilon_{22}\varepsilon_{33}\right) + \left(\frac{\varepsilon_{12}}{S_{12}^{\varepsilon}}\right)^2 + \left(\frac{\varepsilon_{13}}{S_{13}^{\varepsilon}}\right)^2 \quad (\varepsilon_{22}+\varepsilon_{33}) \geq 0 \tag{4}$$

Matrix compressive failure:

$$R_{mc}^2 = \left(\frac{E_{22}\varepsilon_{22}+E_{33}\varepsilon_{33}}{2G_{12}S_{12}^{\varepsilon}}\right)^2 + \left(\frac{\varepsilon_{22}+\varepsilon_{33}}{Y_C^{\varepsilon}}\right)\left[\left(\frac{E_{22}Y_C^{\varepsilon}}{2G_{12}S_{12}^{\varepsilon}}\right)^2 - 1\right] + \left(\frac{1}{S_{23}^{\varepsilon}}\right)^2\left(\varepsilon_{23}^2 - \frac{E_{22}E_{33}}{G_{23}^2}\varepsilon_{22}\varepsilon_{33}\right) + \left(\frac{\varepsilon_{12}}{S_{12}^{\varepsilon}}\right)^2 + \left(\frac{\varepsilon_{13}}{S_{13}^{\varepsilon}}\right)^2 \quad (\varepsilon_{22}+\varepsilon_{33}) \leq 0 \tag{5}$$

Yeh delamination failure:

$$R_{ld}^2 = \left(\frac{\varepsilon_{33}}{Z_T^{\varepsilon}}\right)^2 + \left(\frac{\varepsilon_{13}}{S_{13}^{\varepsilon}}\right)^2 + \left(\frac{\varepsilon_{23}}{S_{23}^{\varepsilon}}\right)^2 \quad (\varepsilon_{33} \geq 0) \tag{6}$$

where X_T^{ε}, X_C^{ε}, Y_T^{ε}, Y_C^{ε}, S_{12}^{ε}, S_{13}^{ε}, S_{23}^{ε} and Z_T^{ε} represent the ultimate strain components in the longitudinal (*X*), transverse (*Y*), and through-thickness (*Z*) direction of the laminate, corresponding to stress strength components listed in Table 3. The failure factor R_i (i = *ft*, *fc*, *mt*, *mc*, *ld*) is the damage threshold parameter to indicate whether or not the damage

begins to initiate. The ultimate strain components are determined in conjunction with the corresponding stress strengths,

$$\begin{aligned} X_T^{\varepsilon} &= X_T / E_{11}, \quad X_C^{\varepsilon} = X_C / E_{11} \\ Y_T^{\varepsilon} &= Y_T / E_{22}, \quad Y_C^{\varepsilon} = Y_C / E_{22}, \quad Z_T^{\varepsilon} = Z_T / E_{33} \\ S_{12}^{\varepsilon} &= S_{12} / G_{12}, \quad S_{13}^{\varepsilon} = S_{13} / G_{13}, \quad S_{23}^{\varepsilon} = S_{23} / G_{23} \end{aligned} \tag{7}$$

Once the individual initiation failure criterion is satisfied $R_i \geq 1.0$, damage evolution begins immediately, which results in a gradual reduction in the composite material stiffness. Thus, the damage variable d_i ranging from 0 to 1 is introduced to depict the current state of the material degradation [50],

$$d_i = 1 - \frac{1}{R_i^n} \quad \left(R_i \geq 1,\ n \geq 1;\ i = ft,\ fc,\ mt,\ mc,\ ld\right) \tag{8}$$

where the subscript "*f*" and "*m*" refer to fiber and matrix, and the subscript "*t*" and "*c*" represent tensile and compression, respectively; the subscript "*ld*" signifies inter-laminar delamination. In accordance with the trial and experimental measure, the control factor is set to one [51, 52]. Since the material damage results in irreversible energy dissipation, the variable d_i is expressed as a function of time *t*,

$$d_i^t = \max\left(d_i^{\tau},\ 0\right) \quad \left(\tau \leq t;\ i = ft,\ fc,\ mt,\ mc,\ ld\right) \tag{9}$$

During the damage evolution stage, the stiffness at this material point needs to be degraded in the damage growth direction and the stresses should be updated according to the constitutive equation. Thus, the damage parameter ω_i $(i = 1, \cdots, 6)$ is introduced to determine the reduce of material stiffness in conjunction with components of undamaged compliance matrix [53]. The constitutive relation between the stress and strain can be expressed more explicitly as follows:

$$\begin{Bmatrix}\varepsilon_{11}\\ \varepsilon_{22}\\ \varepsilon_{33}\\ \gamma_{12}\\ \gamma_{23}\\ \gamma_{13}\end{Bmatrix}=\begin{bmatrix}\frac{1}{E_{11}(1-\omega_1)} & -\frac{\nu_{12}}{E_{22}} & -\frac{\nu_{13}}{E_{33}} & 0 & 0 & 0\\ -\frac{\nu_{12}}{E_{22}} & \frac{1}{E_{22}(1-\omega_2)} & -\frac{\nu_{23}}{E_{22}} & 0 & 0 & 0\\ -\frac{\nu_{13}}{E_{33}} & -\frac{\nu_{23}}{E_{22}} & \frac{1}{E_{33}(1-\omega_3)} & 0 & 0 & 0\\ 0 & 0 & 0 & \frac{1}{G_{12}(1-\omega_4)} & 0 & 0\\ 0 & 0 & 0 & 0 & \frac{1}{G_{23}(1-\omega_5)} & 0\\ 0 & 0 & 0 & 0 & 0 & \frac{1}{G_{13}(1-\omega_6)}\end{bmatrix}\begin{Bmatrix}\sigma_{11}\\ \sigma_{22}\\ \sigma_{33}\\ \tau_{12}\\ \tau_{23}\\ \tau_{13}\end{Bmatrix} \tag{10}$$

where the damage parameter ω_i $(i=1,\cdots,6)$ is defined via the damage variables in initiation failure criteria,

$$\begin{aligned}&\omega_1=\max(0.0,\ d_f), && \omega_2=\max(0.0,\ d_f,\ d_m), && \omega_3=\max(0.0,\ d_f,\ d_d)\\ &\omega_4=\max(0.0,\ d_f,\ d_m), && \omega_5=\max(0.0,\ d_f,\ d_d), && \omega_6=\max(0.0,\ d_f,\ d_d)\\ &d_f=\max(0.0,\ d_{ft},\ d_{fc}), && d_m=\max(0.0,\ d_{mt},\ d_{mc}), && d_d=\max(0.0,\ d_{ld})\end{aligned} \tag{11}$$

4.3 Finite element implementation

The progressive damage model is executed to analyze structural response and to identify failure modes of fiber and matrix in ABAQUS/Explicit in conjunction with a user-defined material VUMAT subroutine. The main execution procedures of the subroutine are illustrated in Fig. 4. At each incremental step, the subroutine is called at each integration point and the time Δt and strain $\Delta\varepsilon$ increment as well as the state variables (stains ε and damage variables d_i) are passed into the VUMAT through the ABAQUS solver. The total strains can be achieved by adding the strain increments of this incremental step and strains of the previous incremental step. Based on the strains, the stresses at each integration point can be computed in accordance with stiffness matrix. Subsequently, failure at any given material point can be checked according to the strains

based on failure criteria. If the damage initiation has occurred, the damage variable can be calculated for each failure mode in the light of the damage evolution law. Then, the constitutive matrix and the stresses can be updated in a sequential manner. The state variables obtained from the subroutine are introduced into ABAQUS solver to proceed the next increment calculation. In the calculation process, the excessively distorted elements will be removed to avoid aborting the calculation and affecting the final results when the principal strain at any integration point reaches a critical value. The above procedure should loop over all the integration points until the end of computation process.

4.4 Finite element model

The implementation process of residual flexural strength after impact can be divided into three steps, as displayed in Fig. 5. The first step represents the low-velocity impact simulation, generating the impact damage under various impact energy levels. The second step is conducted to prepare for the bending simulation, changing the boundary conditions of impact simulation to bending simulation and eliminating oscillation of sandwich beam. The third step represents the bending simulation, performing the whole bending process.

The finite element (FE) model for low-velocity impact simulation is displayed in Fig. 6. The face sheet is modelled with 8-node reduced integration elements (C3D8R) for each laminate layer, and enhanced hourglass control formulation is used to improve computational accuracy. The honeycomb core is discretized with 4-node shell element (S4R). The mesh size is mostly 0.5 mm $\times$ 0.5 mm in the impact region, while biased meshes are applied in the remaining zone. It is found from the experimental results that there is no massive debonding failure in the adhesive interfaces between the honeycomb core and skins for either impact or bending test. Therefore, the interfaces are assumed to

be perfectly bonded and are constrained together accordingly by using the "tie" command in ABAQUS.

For the impact simulation, two steel rings with internal diameter of 75 mm are discretized with C3D8R and are treated as rigid bodied to simulate the clamping boundary conditions. The bottom clamp is fully fixed and the top clamp is constrained all freedom degrees except z-direction. The impactor is discretized with C3D8R as a rigid body and fully constrained except the z-direction. Impact energy can be achieved by the initial velocity, which is assigned as a predefined field variable at the reference point of impactor.

After the impact process completes, it is critical to change the boundary conditions of impact simulation to bending simulation for a consecutive analysis, as illustrated in Fig. 7. The indenter and two supports are discretized with C3D8R as rigid bodies according to experimental conditions. During bending, two supports are constrained all degrees of freedom, and the indenter is only allowed to move along the loading direction. In the bending process, a sinusoidal waveform loading rate (average speed of 1 m/s) is applied through trial and error to achieve a balance of calculation efficiency and accuracy. The state variables obtained from the impact simulation, including the stresses, strains, damage variables, and residual formation of the sandwich beam, are transferred to the bending simulation as the initial states.

5. Results and discussion

To evaluate the effect of impact-induced damage on the impact response and resulting damage state, specimens with four different structural configurations are tested and analyzed systematically under three impact energy levels. Subsequently, three-point bending tests are executed on the impacted specimens to explore the influence of impacted-induced damage on the residual flexural strength. Meanwhile, finite element

analysis is implemented to further investigate the influences of impacted damage on residual flexural properties of such structures under various impact energy levels.

5.1 Low-velocity impact characterization

5.1.1 Low-velocity impact tests

Fig. 8 and 9 depict the impact load-time, load-displacement and absorbed energy-time curves of sandwich panels with four different structural configurations under three impact energy levels. It is well known that the bending stiffness of sandwich panel increases with increasing of cell wall thickness or core height, or with decreasing of cell wall length. The key response parameters such as peak load, absorbed energy and maximum deflection during the impact event are shown in Table. 4. Additionally, the scanning images of face sheet and cross-sectional views through the impact location of the sandwich panels are presented to supply the significant information about the deformation and damage patterns, as described in Fig. 10.

The impactor is rebounded back for the 5 J case due to the elastic recovery of the panel and more than 80% impact energy is absorbed by sandwich panels in the form of composite damage and core deformation. There is no obvious damage but with only barely visible indentation in the impact area of top face sheet. Additionally, there is perhaps matrix cracking occurring in the impact area due to local bending and membrane stretching, and the buckling and folding of cell walls mainly generate around the impact region adjacent to the top face sheet. The impactor partially penetrates the sandwich panel for the 10 J case, and rebounds back with a relatively smaller velocity compared with 5 J cases, so the vast majority of impact energy is absorbed, as described in Fig. 9(b). After the peak load, the prolonged load plateau is associated with further expansion of matrix cracking and fiber breakage for the top face sheet as well as buckling and collapse of the core. The top face sheet exhibits evident indentation along with intricate damage around the impact zone, mainly including fiber fracture, matrix cracking and

delamination (Fig. 10). After the face shear fracture, core crushing and core shear tend to worsen with the impactor continuing to drop down. It is noted that the damage area of specimen T0.06-H10-L1.5 is smallest than others, while the local residual indentation is the deepest one. This is due to the fact that increasing cell wall thickness could enhance the bending stiffness, which results in smaller deformation of the top face sheet around the impactor. The impactor penetrates the whole sandwich panel completely for 50 J case, and the corresponding load curve exhibits double-hump shape with two peak loads. It is found that the second peak load is slightly larger than the first one, which could be not only due to the effect of the friction between the impactor and the failed composite laminate and core, but also the adhesive film between the bottom face sheet and the core.

From the impact load curves, the specimen with cell wall length of 1.5 mm produces the highest peak load, while the specimen with cell wall thickness of 0.04 mm produces the lowest load for the non-perforation cases. It is obviously that the load values in the stable plateau stage are larger for the panel with higher compressive strength or bending stiffness. It can be concluded that the peak load increases with bending stiffness increasing, which indicates that the sandwich panel with higher stiffness offers better impact resistance capacity. Compared specimens T0.06-H10-L3.0 and T0.06-H15-L3.0, the peak forces are almost the same for the non-perforation cases, which indicates that increasing core height has little effect on the impact performance. That is attributed to the fact that there are the same compressive strengths for these two specimens with the identical cores. However, the contact time of specimen T0.06-H10-L3.0 is slightly longer than that of specimen T0.06-H15-L3.0. It can be explained that the global deformation of the latter under the impact loading is smaller than the former due to higher bending stiffness. For the perforation case, the loading ascending phase of the second hump for specimen T0.06-H15-L3.0 occurs later than others, which is due to the fact that the impactor penetrates higher core consuming a relatively longer time. In essence, the local

damage induced by impact loading is limited to the impact zone for all cases, it exhibits the similar failure mechanisms for the impact process. Under the impact loading, the top face sheet is penetrated gradually, along with matrix cracking and fiber breakage; the cell walls of core within the impact zone are sequentially folded and crushed, and the cell walls just outside the deformation region do not experience any buckling and remain perpendicular to the face sheet. Consequently, increasing cell wall thickness or decreasing side length of honeycomb core has significant effects on peak load, while increasing core height has little effect. It can be concluded that the core strength plays a crucial role in the deformation and damage of sandwich structure and further determines its impact resistance.

5.1.2 Simulation of the impact response

Due to the similar failure mechanisms for specimens with different structural configurations, the specimens T0.06-H10-L3.0 and T0.06-H10-L1.5 are modelled to further explore the deformation process and resulting damage state. The predicted impact responses such as impact load and energy absorption curves are compared with the measured ones, indicating reasonably good agreement with each other, as plotted in Fig. 11. Generally, the predicted impact load values are slightly overestimated in comparison with the experiment ones. This could be due to the processing defect of adjacent core cells and the thickness tolerance of composite sheet. It is noteworthy that the sudden load drops and subsequent prolonged load plateaus are also successfully captured by the simulation for the 10 J cases. However, for the penetration cases, the impact load values obtained from the simulation are relatively smaller than experimental results in the region between two peak loads. It is chiefly because the failed materials still exist in the real panel, including broken fibers/matrix and the core, which aggravates the interface friction of the impactor during the penetration process; whereas, the failed elements in the excessive deformation region have been removed from the FE model during the

calculation process, which does not meet reality. To facilitate comparison, the predicted and measured impact parameters such as peak load, absorbed energy and maximum deflection are also compared in Fig. 12. Overall, the maximum errors for peak load, absorbed energy and maximum deflection for all non-penetration and penetration cases are 8.4%, 8.1% and 10.9%, respectively, which are within an acceptable range.

To further reveal the failure mechanisms, solution dependent variables (SDVs) are employed to monitor the damage patterns, such as fiber, matrix and delamination failure. Taking specimen T0.06-H10-L1.5 as an example, the predicted impact damage for each failure mode is exhibited in Fig. 13. When the lower impact energy (5 J) is exerted, the impact load is insufficient to generate obvious penetrative damage (no elements deletion); instead, some damage such as inter-laminar delamination and matrix tensile/compressive damage occurs as the predominant failure patterns in the surrounding impact region. The core around the impact zone is fully intact with marginal crushing and shear failure, which is predicted closely with experimental results. As the impact energy increasing (10 J), there are some elements removed in the impact zone of top face sheet along and perpendicular to the fiber, implying the top face sheet exhibits a severe failure in the form of fiber fracture and matrix cracking, which is similar to the experimental results. Therefore, the dominated failure patterns of the laminate become fiber tensile fracture and matrix tensile/compressive damage instead of delamination, which absorb the vast majority of impact energy. Consequently, the energy absorption mechanisms are closely related with the significant characteristics of failure modes. Under this impact energy level, the profile and size for each failure pattern extend in proportion to the corresponding one for 5 J case. Additionally, core crushing and core shear failure play a role in resisting impact load. For the penetration case, the similar deformation characteristics and failure mechanisms as the 10 J case can be revealed from the

simulation. Overall, the predicted damage states and failure mechanisms show generally fair agreement with the experimental results.

To facilitate the observation of deformation/failure of the panel, the crushing process of specimen T0.06-H10-L1.5 with the von Mises stress contours for the 40 J case is displayed in Fig. 14. As the impactor continues the penetration, the top face sheet at the contact zone is compressed by the impactor in the out-of-plane direction, primarily undergoing local bending and membrane stretching around the impact zone. Meanwhile, the cell walls adjacent to the top face sheet begin to (elastic or plastic) buckling and folding. The top face sheet exhibits a significant indentation whose diameter is larger than the impactor due to gradual deformation of top face sheet. When the strain of damage zone reaches the critical failure strain, a crack forms in the top face sheet. Simultaneously, the core crushing and collapse occur with regularity initiating from the top face sheet along axial direction. It is obvious that the extent of core collapse is not uniform, exhibiting less and less from the center to the periphery. Along with the impactor dropping, the top face sheet, honeycomb core and bottom face sheet are penetrated in a sequential manner.

5.2 Post-impact flexural behavior

5.2.1 Post-impact flexural tests

The influences of impact-induced damage on the residual flexural strength are investigated through a series of non-impacted and impacted specimens with different structural configurations under various impact energy levels. The load-displacement curves of all specimens under bending load are plotted in Fig. 15. According to the variation trend of all curves, it can be concluded that localized damage at the peak load takes place according to the competing failure pattern of face sheet failure and core failure. Fig. 16 displays the two representative load-displacement curves along with failure process images of specimens T0.06-H10-L3 and T0.06-H10-L1.5 under the

impact energy of 10 J, which represent two typical failure patterns (core failure and face sheet failure) potentially induced in the bending tests. Generally, the load-displacement curves can be divided into three distinct stages: the initial elastic stage (Stage I), the core or face sheet failure stage (Stage II), and global failure stage (Stage III). In Stage I, the specimen deforms elastically in the initial phase of bending and the corresponding load value has a nearly linear increase within in a limited loading displacement almost up to the peak load. However, for the core failure case, there is a little non-linearity in the load-displacement curve prior to peak load, indicating some plastic buckling of the core occurring under the indenter. In Stage II, there are two distinct regimes (core failure and face sheet failure) during the bending process, and the trend change is closely associated with the competing failure patterns of sandwich panel. After the top face sheet complete fracture, there is a relative stable load plateau until the final rupture of the panel in Stage III. In this stage, the prominent failure patterns are core crushing under the indenter and further delamination of the fracture section in the top face sheet, therefore load-carrying capacity of the sandwich beam becomes stable.

From the experimental results, the load-displacement curve of specimen T0.06-H10-L1.5 demonstrates obviously different characteristics with other specimens, especially for Stage II (Fig. 16), implying the different failure mechanisms for specimens with different structural configurations under bending load. For the lower core stiffness cases, the core buckling occurs after the peak load (Stage II(a)) whether the specimen is impacted or not, and the load drops slowly; as the indenter moving, the top face sheet fractures (Stage II(b)), and the subsequent load drops sharply. During the bending process, the cell walls of core within the contact zone are sequentially folded and crushed or exhibit shear deformation until the face sheet fracture. For specimen with higher core stiffness (T0.06-H10-L1.5), there is only face sheet failure occurring but without evident core crushing or shear, which is distinctly different with the core failure cases. In reality,

the face sheet failure behaves in a brittle manner. Overall, the core stiffness is closely related to the final failure patterns and failure mechanisms under bending load.

The maximum contact force of the load-displacement curve is considered as the residual flexural strength of post-impact sandwich panel, which is an important indicator to evaluate the carrying capacity of the damaged specimen. To intuitively explore the influence of impact damage, the normalized residual flexural strength is deemed as the ratio of bending strength of damaged panel to that of the corresponding undamaged one. The residual flexural strength and corresponding normalized strength of sandwich panels with different structural configurations as a function of the impact energy level have been described in Fig. 17. Obviously, the residual flexural strength increases with the increasing of compressive strength or bending stiffness whether the specimen is impacted or not. Consequently, the specimen failing by top face sheet fracture exhibits higher residual flexural strength than that failing by core crushing. As would be expected, the residual bending strength decreases for the impacted specimens with the increasing of impact energy. The reduction in residual bending strength is different for specimens with various structural configurations under the same impact energy. The detailed residual bending behavior and failure mechanism for each kind of specimen will be illuminated in the following:

(a) residual bending behavior of specimen T0.06-H10-L3

Specimen T0.06-H10-L3 is chosen as a reference to identify the influence of structural configurations on the residual flexural strength, and its bending failure characteristics and damage mechanisms under various impact energy levels are described in more detail in the following section. Compared with the load-displacement curves in Fig. 15(a), it is found that these curves seem to have roughly similar characteristics whether the specimens are impacted or not, implying the similar underlying damage mechanisms for specimens under flexural loading. As a matter of fact, collapse mode is independent of

the extent of the impact-induced damage, while it has a huge effect on the residual flexural strength. For the perforation case, the residual flexural strength reduces to 75% compared with the non-impacted one. With respect to the bending stiffness, it is somewhat less sensitive to the impact-induced damage in comparison with the residual flexural strength, especially for the lower impact energy cases (5 J). In fact, the bending stiffness represents the slope of load-displacement curve for the entire sandwich panel, while the residual flexural strength indicates the maximum contact force exerted on the local damaged zone. The local damage induced by impact loading is limited to the impact zone, thus it has far less influence to global properties such as bending stiffness. There is a relatively large variation of the bending stiffness for the case with larger core stiffness after the top face sheet suffered serious damage (10 J).

Under the bending load, the top face sheet of sandwich panel is subjected to the compressive stress, while the bottom face sheet suffers from the tensile stress. As the increasing of the bending load, the core buckling occurs initiating in the contact area with the indenter (Fig. 18(a)), and the load drops slowly. As the indenter moving to 4 mm, a sharp load drop emerges, indicating the onset of initial damage in the top face sheet in the form of matrix cracking and fiber fracture; the subsequent load drops are associated with progressive matrix and fiber damage. Essentially, when the stress concentration of the top face sheet under the indenter reaches the compressive failure strength, a clear crack occurs, which is mainly induced through the compressive fiber failure with a loud audible sign. The typical damage images of non-impacted and impacted specimens under 10 J impact energy are illustrated in Fig. 19. The final failure of the top face sheet is featured by a crack with fiber fracture spanning the whole face sheet whether the panel is impacted or not. However, the formation process of crack in the top face sheet could has some differences between the non-impacted and impacted panels. For the non-impacted panel, the cracks could initiate from both free edges of the top face sheet in the contact

zone with the indenter, and propagate rapidly to the center of the face along a straight line with the increasing of compressive stress. However, for the impacted panel, the cracks are generated spontaneously initiating from the damage zone in the top face sheet, and further extend to both edges of the face sheet, which is similar with the finding of the corrugated core sandwich structure suffered impact loading [40]. In summary, the failure mechanisms are fairly similar whether the panel is impacted or not, although different crack initiation site exists in the top face sheet.

(b) influence of cell wall thickness

For the non-impacted specimen, the load exhibits a sharp drop followed by a lower but fairly prolonged load plateau after the peak load, as displayed in Fig. 15(b). This drop could be due to the fact that the weak core begins to be local buckling and then crushing under the compression of indenter (Fig. 18(b)), which further results in a premature failure in overall ultimate bearing capacity of the structure. After the load drop, the specimen deforms stably in the form of progressive crushing and shear of the core which accommodates local deformation of top face sheet. For the impacted specimen, the load increases slowly after the elastic stage, which is due to the fact that core buckling begins to take place around the impact zone and further aggravates global bending deflection.

Compared with the specimen T0.06-H10-L3.0, it is found that there is a noticeable decrease in the residual flexural strength as the cell wall thickness becomes thinner, especially for the impacted specimens. In the context of the same impact energy, the residual flexural strength of specimen T0.04-H10-L3.0 is about 35% lower than that of specimen T0.06-H10-L3.0. Furthermore, the residual flexural strength of the 5 J case reduces 27% in comparison of the non-impacted specimen. It can be explained that the inter-laminar delamination and matrix cracking have been induced by the impactor in the top face sheet even under a lower impact energy level (5 J), and the damage is prone to grow under compressive stress, which results in the residual flexural strength of impacted

specimen diminishing markedly compared with the non-impacted one. This further illustrates that the top face sheet plays a vital role in overall ultimate bearing capacity of the structure under the bending load.

(c) influence of honeycomb core height

The collapse mode of specimen T0.04-H15-L3.0 is similar with specimen T0.04-H10-L3.0, featured by a mixed failure of core crushing and shear before the face sheet fracture, as illustrated in Fig. 15(c). After the peak load, there is a sudden load drop due to the core buckling for the non-impacted specimen; and then, it exhibits a stable load plateau along with progressive core crushing and shear under the indenter (Fig. 18(c)). However, the face sheet fracture occurs earlier (about 4 mm) than the specimen T0.04-H10-L3.0 (after 6 mm). This could be attributed to the fact that the bending stiffness increases with the increasing of cell wall thickness, which results in smaller global bending deflection and deeper local indentation, as exhibited in Fig. 18(c); so the deformation of top face sheet is more localized, leading to the top face sheet breaking earlier. For the impacted specimen, the collapse mode of impacted specimen exhibits a fairly similar pattern to that of impacted specimen T0.04-H10-L3.0, but with smaller global bending deflection.

Compared with the specimen T0.06-H10-L3.0, it is found that the peak load for non-impacted specimen is roughly 32% higher, whereas about 8% higher for the impacted ones. It is evident that the peak load is sensitive to the core height, especially for the non-impacted specimen, due to the bending stiffness is drastically affected by the core height. Although increasing the core height has little effect on the low-velocity behavior, its benefits will be more pronounced for residual flexural strength.

(d) influence of cell wall length

Specimen T0.06-H10-L1.5 fails through top face sheet fracture, which is distinctly different with the core failure cases. For this specimen, the face sheet failure behaves in a

brittle manner with unnoticeable non-linearity in the load-displacement curve prior to failure, and then a sudden load drop occurs followed by a prolonged load plateau (Fig. 15(d)). After the elastic stage, the face sheet breaks abruptly in about 3.5 mm (Fig. 18(d)) whether the specimen is impacted or not, and then the load drops drastically to a lower value (about 1 kN). Compared with the core failures cases, the specimen failing by face sheet fracture exhibits better ultimate load-bearing capacity.

Compared with the specimen T0.06-H10-L3.0, it is found that the peak load for the non-impacted specimen is roughly 124% higher, whereas about 95% higher for the impacted ones. Indeed, increasing the core stiffness could improve the residual flexural strength. Different structural configurations of cores result in different failure modes, and further affect the residual flexural strength pronouncedly. Overall, the structural configurations such as cell wall thickness, core height and cell side length play a crucial role in determining failure mechanisms during bending, which in turn might lead to significantly different residual flexural strength.

5.2.2 Theoretical solutions for the bending test

Theoretical analyses are carried out to determine the peak bending loads of non-impacted specimens according to the initial failure mode occurring right at the peak load. As observed in previous section, two competing failure patterns of sandwich beams, namely core buckling and face sheet fracture, appear in the present experimental range. As for initial failure mode of core buckling, the simplified formula for predicting the peak bending load of such structures can be expressed as [54],

$$P_c = \frac{2bt^2}{L}\sigma_{yf} + 2bc\tau_{yf}\left(1+\frac{2S}{L}\right) \tag{12}$$

where b, L are the width and span of sandwich beam, t, c are the thickness of face sheet and core, respectively, and S is the overhanging length of beam; σ_{yf}, τ_{yf} are the yield strength of face sheet and shear strength of core, respectively.

The bending moment of simply supported sandwich beam should be calculated by integrating the first moment of bending stress, considering the shear effects due to core on the resistive bending moment [55],

$$M = C\frac{bh^2\sigma_f}{4}\left[1-\left(\frac{c}{h}\right)^2\right] = \frac{PL}{4} \tag{13}$$

where $h = 2t + c$, C is shear effect factor,

$$C = \frac{C_1}{C_1 + C_2} \tag{14}$$

where $C_1 = \frac{L^3}{48(\mathrm{EI})_{eq}}$, $C_2 = \frac{L}{4(\mathrm{AG})_{eq}}$.

The equivalent bending rigidity $(\mathrm{EI})_{eq}$ and shear rigidity $(\mathrm{AG})_{eq}$ are expressed as,

$$(\mathrm{EI})_{eq} \approx \frac{E_f btc^2}{2},\ (\mathrm{AG})_{eq} = G_c bc \tag{15}$$

where E_f represents the Young's modulus of face sheet; G_c represents the shear modulus of core. As for initial failure mode of face sheet fracture, the critical bending load of such structures can be obtained when the bending stress reaches the compressive strength of face sheet. So, the critical bending load can be expressed as,

$$P_f = C\frac{bh^2\sigma_{yf}}{L}\left[1-\left(\frac{c}{h}\right)^2\right] \tag{16}$$

The comparisons of peak load between theoretical solutions and experimental results for non-impacted specimens are listed in Table 5. These theoretical and experimental results are in reasonably good agreement with the maximum error of 8.7% for specimen T0.06-H10-L3.0.

5.2.3 Simulation of residual flexural behaviour

Specimens T0.04-H10-L3.0 and T0.06-H10-L1.5 are chosen to further investigate the post-impact failure mechanisms and residual flexural strength, because they behave two typical failure modes (core failure and face sheet failure). Fig. 20 displays the comparison of numerical and experimental load-displacement curves of specimens T0.04-H10-L3.0 and T0.06-H10-L1.5, indicating reasonably good agreement with each other in terms of structural stiffness and peak load. The structural stiffness of each specimen is also successfully captured by the numerical simulation whether the specimen is impacted or not. For the post-impact specimen, the predicted sudden load drop occurs later than the measured one. This can be explained that manufacturing defects, such as the material imperfection and uneven thickness of the core and face sheets, are not considered in the numerical model; additionally, inter-laminar delamination and matrix cracking induced by the impactor in the top face sheet are vulnerable to generate progressive damage under the compression loading in test. For specimens failing by core crushing (T0.04-H10-L3.0), the predicted load values in the prolonged stage are slightly overestimated compared with the measured ones for the post-impact specimens. This could be attributed to the fact that two fracture surfaces formed after the face sheet complete breaking take place offset intersection in test, while the phenomenon of offset intersection does not appear in the numerical model; on the other hand, the localized interface debonding impairs the transfer of traction between the face sheet and core, which further results in a decrease in bending stiffness of the beam. Moreover, for the Explicit analysis, there are some oscillations occurring in the loading ascending phase of predicted load-displacement curve, which is attributed to the vibration of slender beam with simply supported boundary conditions in the initial loading stage; after the top face sheet fracture exhibits some oscillations, which indicates the damage process of laminates (damaged elements deletion). The numerical and experimental peak loads (residual

flexural strength) are summarized in Fig. 21, which match well with each other. The maximum error for the peak load is 5.6% for specimen T0.06-H10-L1.5 under 5 J impact energy. It can be concluded that the integrated FE model is highly effective to predict the residual flexural properties of the post-impact sandwich panel.

With respect to the predicted collapse patterns, specimens with different structural configurations exhibit different failure modes under the bending load. Specimen T0.06-H10-L3.0 fails by undergoing core buckling firstly and then top face sheet fracture, while specimen T0.06-H10-L1.5 fails abruptly through top face sheet fracture, which is fairly similar with the experimental results. As an example, the crushing process of specimen T0.06-H10-L3.0 with Mises stress contours is illustrated in Fig. 22. As far as the core failure concerned, the Hertz pressure on the core generated by the indenter distributes in an elliptical pattern in the elastic stage (before 2.5 mm), which determines the initial failure zone. When the pressure reaches to a critical peak load, the buckling of cell walls occurs initiating from the top face sheet in the contact area. As the indenter continues to drive down, the core cell walls gradually crush and the damage area becomes larger than the contact zone because of the face sheet deformation, which is similar with the experimental observation. Regarding to the face sheet, when the compressive strain of the top face sheet reaches the critical failure strain, a crack forms spanning the width of face sheet, which is also successfully captured in the simulation analysis, as illustrated in Fig. 23. The final failure patterns of the top face sheet are brittle compression fracture of fibers along with the inter-laminar delamination and matrix cracking. The top face sheet fracture largely reduces load bearing capacity and further exacerbates localized core crushing under the indenter. As the load displacement of indenter increasing, the extent of core crushing increases toward complete failure.

The comparison of predicted failure modes for the top face sheet after impact and subsequent bending is also exhibited in Fig. 23. The damage for each failure mode

induced by the impact does not propagate obviously during the bending process, especially for the zone away from the crack. Instead, the matrix damage and fiber fracture induced by the compressive stress are the primary failure pattern for the top face sheet for the bending process. After impact, the core crushing only generates around the impactor, and other cell walls exhibit almost barely visible deformation; during the bending process, the global core crushing spanning the panel occurs under the indenter after the face sheet fracture. Finally, plastic collapse of the core generates at the mid-span of the sandwich panel to sustain the compression loading of the indenter, which is fairly similar to the experimental results. Overall, the predicted failure patterns of the post-impact sandwich structure under bending load are reasonably well agreement with the actual damage observed experimentally.

Additionally, two numerical cases (T0.06-H10-L3.0-10J and T0.06-H10-L1.5-10J) for loading applied on the opposite surface of impacted side are chosen to investigate the effect of impact site on the residual flexural strength, as exhibited in Fig. 24. For this case, the indenter directly acts on the intact part of sandwich beam. The top face sheet (intact part) is subjected to compressive stress, while the bottom face sheet (damaged face induced by impact) suffers from tensile stress. Specimen T0.06-H10-L3.0-10J fails through core buckling and crushing under the bending load, while specimen T0.06-H10-L1.5-10J fails by top face sheet fracture even though this face sheet is not subjected to impact damage, which is similar with the specimen applied loading on the impacted side. Furthermore, the bending stiffness is almost the same prior to damage initiation of Stage II. However, the residual flexural strength for specimen impacted on bottom face sheet is larger than that impacted on top face sheet, which is attributed to the fact that the top face sheet and core in the contact zone are not subjected to serious impact damage. It can be concluded that the post-impacted sandwich beam shows higher ultimate bearing capacity for the bending load applied on the relatively intact face sheet.

6. Conclusions

This paper aims to investigate the influences of impact-induced damage on the residual flexural strength of honeycomb core sandwich panels with different structural configurations. A series of low-velocity impact tests and three-point bending tests after impact are carried out to explore impact response and residual flexural behavior of such structures considering different core configurations and various impact energy levels. Subsequently, an integrated FE model with the VUMAT subroutine in ABAQUS/Explicit is developed to further investigate the damage states and failure mechanisms for the impact and bending. The following conclusions can be summarized:

(1) Increasing cell wall thickness or decreasing side length of honeycomb core has significant effects on the impact resistance performance of honeycomb structures, whereas increasing core height has little effect on the peak load.

(2) For the impact-induced damage, the predominant failure patterns exhibit inter-laminar delamination and matrix damage of top face sheet and plastic buckling of core for lower impact energy (5 J); while the dominated failure patterns exhibit fiber fracture and matrix cracking of impacted face sheet as well as core crushing and shear for higher impact energy.

(3) During the bending process, the load-displacement curve can be divided into three distinct stages: the initial elastic stage, the core or face sheet failure stage, and global failure stage. Furthermore, the top face sheet plays a vital role in overall ultimate bearing capacity of the sandwich structure under the bending load.

(4) Specimens with lower core stiffness fail through core buckling and crushing under the bending load whether the specimens are impacted or not, while specimen with higher core stiffness fails by top face sheet fracture. The core stiffness is strongly related to the competing failure pattern (face sheet failure or core failure) under the bending load.

(5) The residual flexural strength reduces 20%-30% (except T0.06-H10-L3.0) even through the superficial impact damage remains barely visible, while there is a minor variation even for the penetration case. Therefore, the residual flexural behaviors have a strong correlation with impact energy and structural configurations of specimens.

(6) The numerical results match well with the experimental ones in terms of impact load, absorbed energy, residual flexural strength and failure modes, which shows that an integrated model with three consecutive steps is a very powerful tool in investigating residual behaviors of sandwich structure after impact.

Acknowledgements

The present work is supported by the National Natural Science Foundation of China (Grant Nos. 51609089 and 51879248), the China Postdoctoral Science Foundation (Grant No. 2016M592338), National Science Fund for Distinguished Young Scholars (No. 51625902), the Offshore Flexible Pipe Project from Ministry of Industry and Information Technology (Nos. 931648030), and the Taishan Scholars Program of Shandong Province (TS201511016).

Appendix A. Effect analysis of loading speed

In order to reduce computational time, a relatively higher loading speed for bending simulation is adopted in dynamic Explicit analysis. A series of sinusoidal waveform loading rates (average velocity 0.5 m/s, 1 m/s, 1.5 m/s and 2 m/s) are chosen to further explore the effect of loading speed. Taking specimen T0.06-H10-L3.0-00J as an example, the predicted load-displacement curves under different loading rates are well consistent with each other in terms of bending stiffness and peak load, as shown in Fig. A.1. However, it is obviously that numerical oscillation phenomenon is more serious for higher loading rate, particularly for the case of 2 m/s. Therefore, the selected loading rate for bending simulation is 1 m/s to balance computational time and accuracy.

References

[1] Birman V, Kardomateas GA. Review of current trends in research and applications of sandwich structures. Compos B Eng 2018;142:221–40.

[2] Du B, Chen LM, Tan JY, Zhou H, Zhao Y, Wu WJ, Li WG, Fang DN, Chen LL. Fabrication and bending behavior of thermoplastic composite curved corrugated sandwich beam with interface enhancement. Int J Mech Sci 2018;149:101–11.

[3] He WT, Liu JX, Tao B, Xie D, Liu JY, Zhang M. Experimental and numerical research on the low velocity impact behavior of hybrid corrugated core sandwich structures. Compos Struct 2016;158:30–43.

[4] Meo M, Vignjevic R, Marengo G. The response of honeycomb sandwich panels under low-velocity impact loading. Int J Mech Sci 2005;47:1301–25.

[5] Zhu GH, Sun GY, Yu H, Li SF, Li Q. Energy absorption of metal, composite and metal/composite hybrid structures under oblique crushing loading. Int J Mech Sci 2018;135:458–83.

[6] Sahu SK, Badgayan ND, Samanta S, Sahu D, Sreekanth PSR. Influence of cell size on out of plane stiffness and in-plane compliance character of the sandwich beam made with tunable PCTPE nylon honeycomb core and hybrid polymer nanocomposite skin. Int J Mech Sci 2018;148:284–92.

[7] Sun G, Huo X, Chen D, Li Q. Experimental and numerical study on honeycomb sandwich panels under bending and in-panel compression. Mater Des 2017;133:154–68.

[8] Liu JX, He WT, Xie D, Tao B. The effect of impactor shape on the low-velocity impact behavior of hybrid corrugated core sandwich structures. Compos Part B Eng 2017;111:315–31.

[9] Chen Y, Fu KK, Hou SJ, Han X, Ye L. Multi-objective optimization for designing a composite sandwich structure under normal and 45° impact loadings, Compos. Part B Eng. 2018;142:159–170.

[10] Shim V, Yang L. Characterization of the residual mechanical properties of woven fabric reinforced composites after low-velocity impact. Int J Mech Sci 2005;47(4–5):647–65.

[11] He WT, Liu JX, Wang SQ, Xie D. Low-velocity impact behavior of X-Frame core sandwich structures – Experimental and numerical investigation. Thin-Walled Struct 2018;131:718–35.

[12] Chen D, Sun G, Meng M, Li G, Li Q. Residual crashworthiness of CFRP structures with pre-impact damage - An experimental and numerical study. Int J Mech Sci 2018;149:122–35.

[13] Bazli M, Ashrafi H, Jafari A, Zhao XL, Gholipour H, Oskouei AV. Effect of thickness and reinforcement configuration on flexural and impact behaviour of GFRP laminates after exposure to elevated temperatures. Compos Part B Eng 2019;157:76–99.

[14] Santiuste C, Sanchez-Saez S, Barbero E. Residual flexural strength after low-velocity impact in glass/polyester composite beams. Compos Struct 2010;92:25–30.

[15] Baran I, Weijermars W. Residual bending behaviour of sandwich composites after impact. J Sandw Struct Mater 2018; 0(0):1–21.

[16] Abir M, Tay T, Ridha M, Lee H. Modelling damage growth in composites subjected to impact and compression after impact. Compos Struct 2017;168:13–25.

[17] Zhang A, Lu H, Zhang D. Effects of voids on residual tensile strength after impact of hygrothermal conditioned CFRP laminates. Compos Struct 2013;95:322–7.

[18] Zhang ZY, Richardson MOW. Low velocity impact induced damage evaluation and its effect on the residual flexural properties of pultruded GRP composites. Compos Struct 2007;81:195–201.

[19] Sarasini F, Tirillo J, D'Altilia S, Valente T, Santulli C, Touchard F, et al. Damage tolerance of carbon/flax hybrid composites subjected to low velocity impact. Compos Part B Eng 2016;91:144–53.

[20] Rivallant S, Bouvet C, Abi Abdallah E, Broll B, Barrau J-J. Experimental analysis of CFRP laminates subjected to compression after impact: the role of impact-induced cracks in failure. Compos Struct 2014;111:147–57.

[21] Caminero MA, Garcia-Moreno I, Rodriguez GP. Damage resistance of carbon fibre reinforced epoxy laminates subjected to low velocity impact: effect of laminate thickness and ply-stacking sequence. Polym Test 2017;63:530–41.

[22] Ghelli D, Minak G. Low velocity impact and compression after impact tests on thin carbon/epoxy laminates. Compos Part B Eng 2011;42:2067–79.

[23] Schubel P, Luo J, Daniel I. Impact and post impact behavior of composite sandwich panels. J Compos: Part A 2007;38:1051–7.

[24] Yang B, Wang ZQ, Zhou LM, Zhang JF, Tong LL, Liang WY. Study on the low-velocity impact response and CAI behavior of foam-filled sandwich panels with hybrid facesheet. Compos Struct 2015;132:1129–40.

[25] de Freitas M, Reis L. Failure mechanisms on composite specimens subjected to compression after impact. Compos Struct 1998;42(4):365–73.

[26] Tian Z, Swanson SR. Residual tensile strength prediction on a ply-ply-ply basis for laminates containing impact damage. J Compos Mater 1992;26(8):1193–206.

[27] Wang SX, Wu LZ, Ma L. Low-velocity impact and residual tensile strength analysis to carbon fiber composite laminates. Mater Des 2010;31:118–25.

[28] El-zein MS, Reigsnider KL. On the prediction of tensile strength after impact of composite laminates. J Compos Tech Res 1990;12(3):147–54.

[29] Wang J, Callinan R. Residual strengths of composite structures subjected to ballistic impact. Compos Struct 2014;117:423–32.

[30] Caprino G, Teti R. Impact and post-impact behavior of foam core sandwich structures. Compos Struct 1994;29(1):47–55.

[31] Wang B, Wu LZ, Ma L, Feng JC. Low-velocity impact characteristics and residual tensile strength of carbon fiber composite lattice core sandwich structures. Compos Part B Eng 2011;42(4):891–7.

[32] Liu Q, Guo O, Ju Y, Lin Y, Li Q. Impact responses and residual flexural properties of narrow CFRP laminates. Compos Struct 2014;111:332–9.

[33] Vachon PL, Brailovski V, Terriault P. Impact-induced damage and damage propagation under flexural load in TiNi and Kevlar-stitched carbon/epoxy laminates. Compos Struct 2013;100:424–35.

[34] Xue LZ, Li KZ, Jia Y, Zhang SY. Hypervelocity impact behavior and residual flexural strength of C/C composites. Vacuum 2017;144:101–6.

[35] Petrucci R, Santulli C, Puglia D, Nisini E, Sarasini F, Tirillò J, et al. Impact and post-impact damage characterisation of hybrid composite laminates based on basalt fibres in combination with flax, hemp and glass fibres manufactured by vacuum infusion. Compos Part B Eng 2015;69:507–15.

[36] Sarasini F, Tirillo J, Valente M, Ferrante L, Cioffi S, Iannace S, et al. Hybrid composites based on aramid and basalt woven fabrics: impact damage modes and residual flexural properties. Mater Des 2013;49:290–302.

[37] Wang X, Hu B, Feng Y, Liang F, Mo J, Xiong J, et al. Low Velocity Impact Properties of 3D Woven Basalt/Aramid Hybrid Composites, Compos Sci Technol 2008;68:444–50.

[38] Hart KR, Chia PXL, Sheridan LE, Wetzel ED, Sottos NR, White SR. Comparison of compression-after-impact and flexure-after-impact protocols for 2D and 3D woven fiber-reinforced composites. Compos Part A 2017;101:471–9.

[39] Klaus M, Reimerdes HG, Gupta NK. Experimental and numerical investigations of residual strength after impact of sandwich panels. Int J Impact Eng 2012;44:50–8.

[40] He WT, Liu JX, Wang SQ, Xie D. Low-velocity impact response and post-impact flexural behavior of composite sandwich panels with corrugated cores. Compos Struct 2018;189:37–53.

[41] Khan MA, Syed AK, Ijaz H, Shah RMBR. Experimental and numerical analysis of flexural and impact behaviour of glass/pp sandwich panel for automotive structural applications. Adv Compos Mater 2018;27(4):367–86.

[42] Wang JF, Shi CY, Yang N, Sun HN, Liu YQ, Song BY. Strength, stiffness, and panel peeling strength of carbon fiber-reinforced composite sandwich structures with aluminum honeycomb cores for vehicle body. Compos Struct 2018;184:1189–96.

[43] ASTM D7136/D7136M-2015. Standard test method for measuring the damage resistance of a fiber-reinforced polymer matrix composite to a drop-weight impact event. ASTM International: West Conshohocken, PA; 2015.

[44] ASTM International. Standard test methods for flexural properties of unreinforced and reinforced plastics and electrical insulating materials. In: D790. West Conshohocken: ASTM International; 2007.

[45] Tsai SW. Strength theories of filamentary structures fundamental aspects of fibre reinforced plastic composites. New York: Wiley-Interscience; 1968. p. 3–11.

[46] Hashin Z. Failure criteria for unidirectional fiber composites. J Appl Mech 1980;47(2):329–34.

[47] Dear JP, Lee H, Brown SA. Impact damage processes in composite sheet and sandwich honeycomb materials. Int J Impact Eng 2005;32:130–54.

[48] Menna C, Manes Zinno A, Asprone D, Prota A. Numerical assessment of the impact behavior of honeycomb sandwich structures. Compos Struct 2013;106:326–39.

[49] Yu GC, Wu LZ, Ma L, Xiong J. Low velocity impact of carbon fiber aluminum laminates. Compos Struct 2015;119:757–66

[50] Huang CH, Lee YJ. Experiments and simulation of the static contact crush of composite laminated plates. Compos Struct 2003;61:265–70.

[51] Zhang GQ, Wang B, Ma L, Xiong J, Yang JS, Wu LZ. The residual compressive strength of impact-damaged sandwich structures with pyramidal truss cores. Compos Struct 2013;105:188–98.

[52] Zhang GQ, Wang B, Ma L, Xiong J, Wu LZ. Response of sandwich structures with pyramidal truss cores under the compression and impact loading. Compos Struct 2013;100:451–63.

[53] Xiao JR, Gama BA, Gillespie Jr JW. Progressive damage and delamination in plain weave S-2 glass/SC-15 composites under quasi-static punch-shear loading. Compos Struct 2007;78:182–96.

[54] McCormack T, Miller R, Kesler O, Gibson L. Failure of sandwich beams with metallic foam cores. Int J Solid Struct 2001;38(28):4901–20.

[55] Paik JK, Thayamballi AK, Kim GS. The strength characteristics of aluminum honeycomb sandwich panels. Thin-Walled Struct 1999;35(3):205–31.

LIST OF TABLES

TABLES

Table 1

Material properties of AA3003 aluminum alloy foil.

Density	Young's modulus	Poisson's ratio	Yield strength
2680 kg/m^3	69 GPa	0.3	116 MPa

Table 2

Structural parameters of the investigated sandwich panels.

Specimen label	Face sheet thickness T_f (mm)	Cell wall thickness T_c (mm)	Core height H_c (mm)	Cell side length L_c (mm)
T0.06-H10-L3.0	1.0	0.06	10	3.0
T0.04-H10-L3.0	1.0	0.04	10	3.0
T0.06-H15-L3.0	1.0	0.06	15	3.0
T0.06-H10-L1.5	1.0	0.06	10	1.5

Table 3

Material properties of the unidirectional laminate.

Symbol	Property	Value
E_{11}	Longitudinal stiffness	108 GPa
E_{22}	Transverse stiffness	8.0 GPa
E_{33}	Out-of-plane stiffness	8.0 GPa
ν_{12}, ν_{13}	Poisson's ratio	0.32
ν_{23}	Poisson's ratio	0.3
G_{12}, G_{13}	Shear modulus	4 GPa
G_{23}	Shear modulus	3 GPa
X_t	Longitudinal tensile strength	2100 MPa
X_c	Longitudinal compressive strength	720 MPa
Y_t	Transverse tensile strength	25 MPa
Y_c	Transverse compressive strength	120 MPa
Z_t	Out-of-plane tensile strength	50 MPa
S_{12}, S_{23}, S_{13}	Shear strength	40 MPa
ρ	Density	1560 kg/m^3

Table 4

Impact response characteristics of the investigated sandwich panels.

Specimen	5 J			10 J			40 J		
	P_L	E_A	D_M	P_L	E_A	D_M	P_L	E_A	D_M
T0.04-H10-L3.0	1.93	4.35	4.61	2.25	10.52	7.72	2.35	34.75	31.94
T0.06-H10-L3.0	2.18	3.95	3.96	2.18	10.43	7.32	2.45	35.34	31.56
T0.06-H10-L1.5	2.85	4.03	3.22	2.68	10.49	5.67	2.96	41.44	25.08
T0.06-H15-L3.0	2.17	4.55	3.86	2.21	10.12	7.01	2.16	38.85	31.00

P_L—Peak load (kN); E_A—Energy absorption (J); D_M—Maximum deflection (mm).

Table 5

The comparison of peak load for non-impacted specimens.

Specimen	Theoretical	Experimental	error
T0.06-H10-L3.0	2.95	2.93	0.7%
T0.04-H10-L3.0	2.27	2.43	6.5%
T0.06-H15-L3.0	4.21	3.87	8.7%
T0.06-H10-L1.5	6.63	6.56	1.1%

LIST OF FIGURES

FIGURES

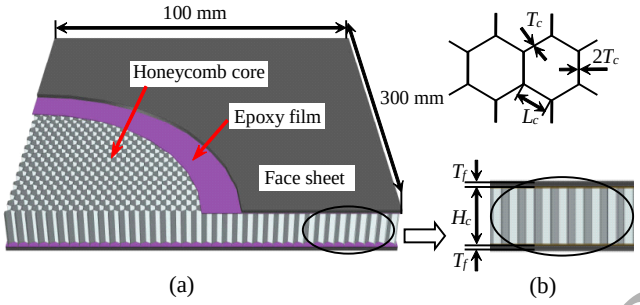

Fig. 1. Schematic of geometric configurations of honeycomb sandwich panel: (a) Dimensions of specimen; (b) Parameters of face sheets and honeycomb cells.

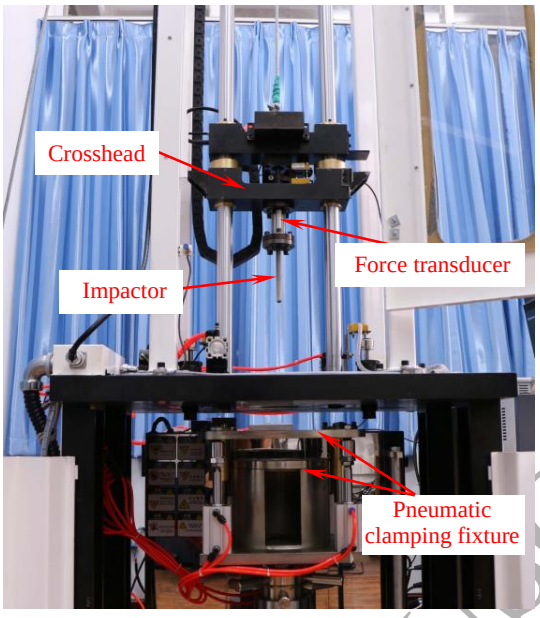

Fig. 2. Schematic of the low-velocity impact test setup.

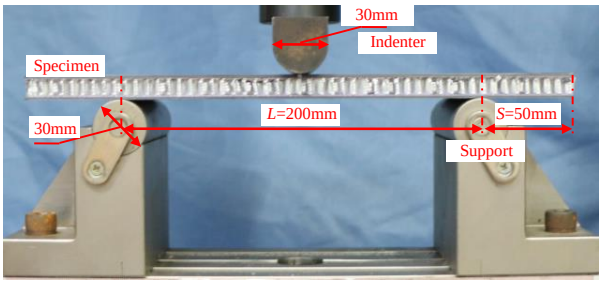

Fig. 3. Schematic of experimental setup for the three-point bending (TPB) tests.

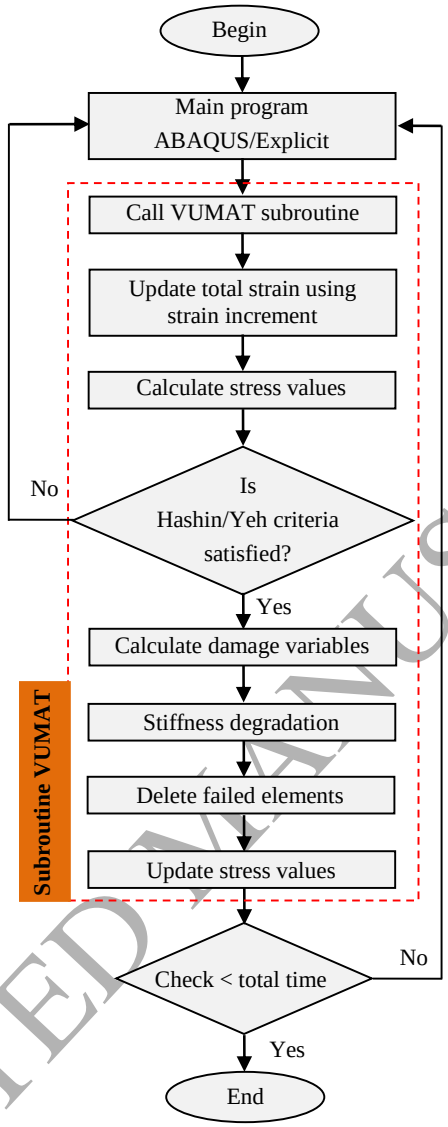

Fig. 4. Flowchart for numerical process of the VUMAT subroutine in ABAQUS.

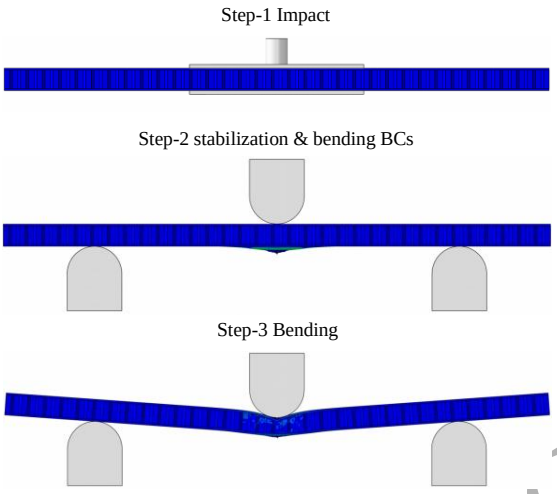

Fig. 5. Integrated FE analysis steps for the simulation.

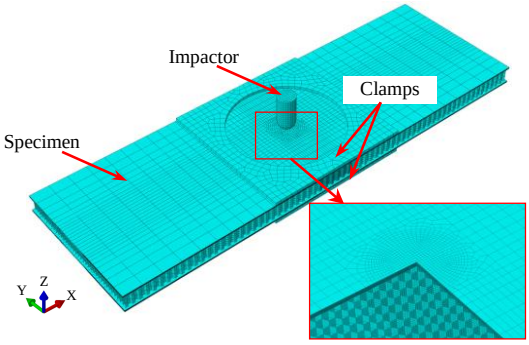

Fig. 6. Finite element model of the low-velocity impact simulation.

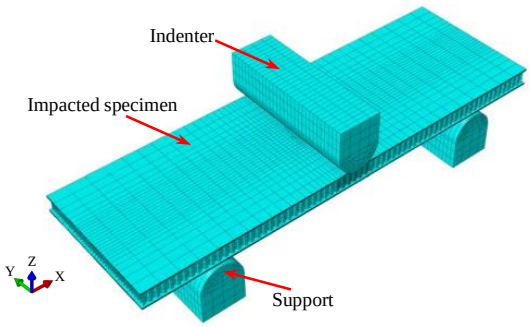

Fig. 7. Finite element model of the residual flexural simulation after impact.

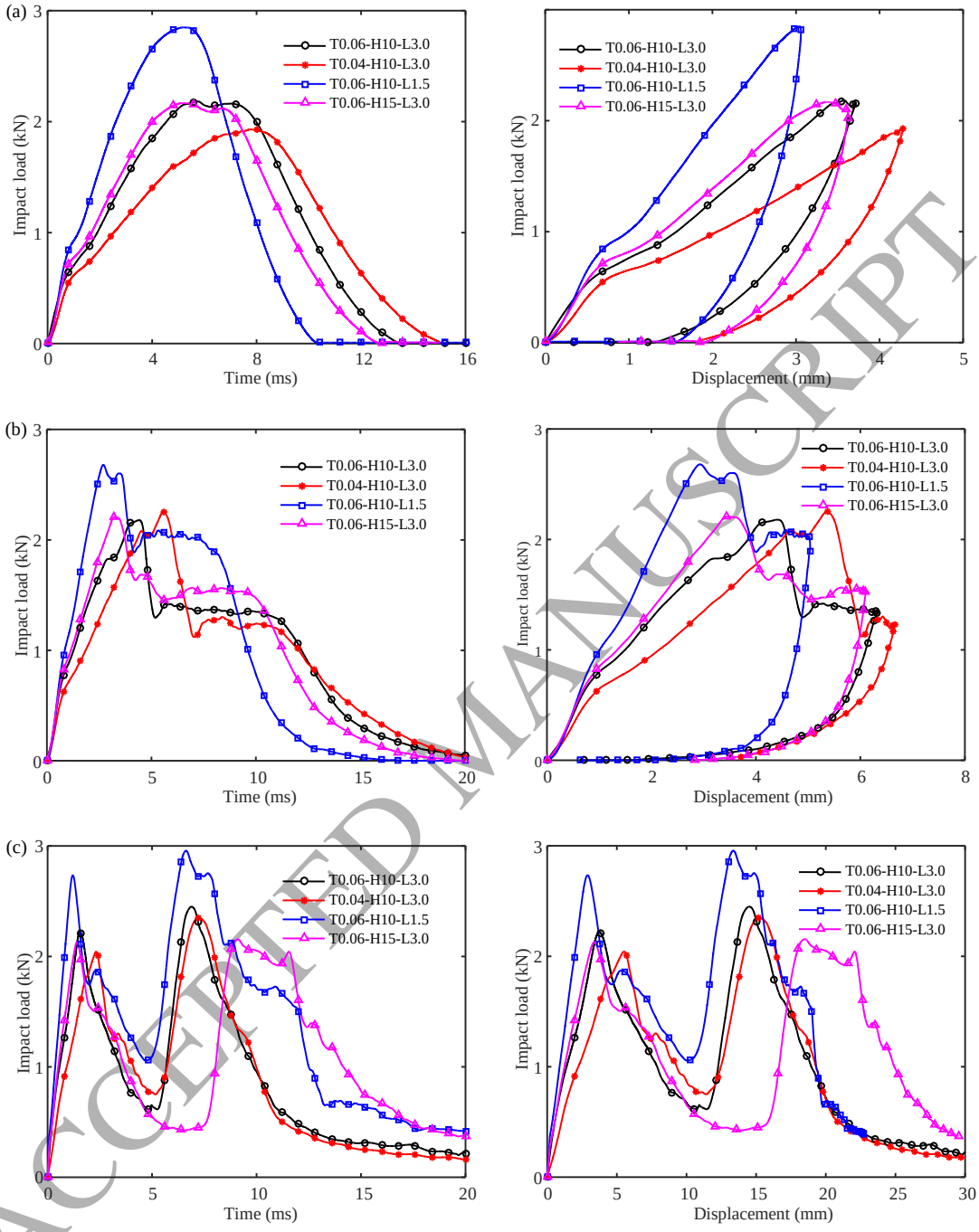

Fig. 8. Impact load-time and load-displacement curves of specimens under various impact energy levels: (a) 5 J; (b) 10 J; (c) 40 J.

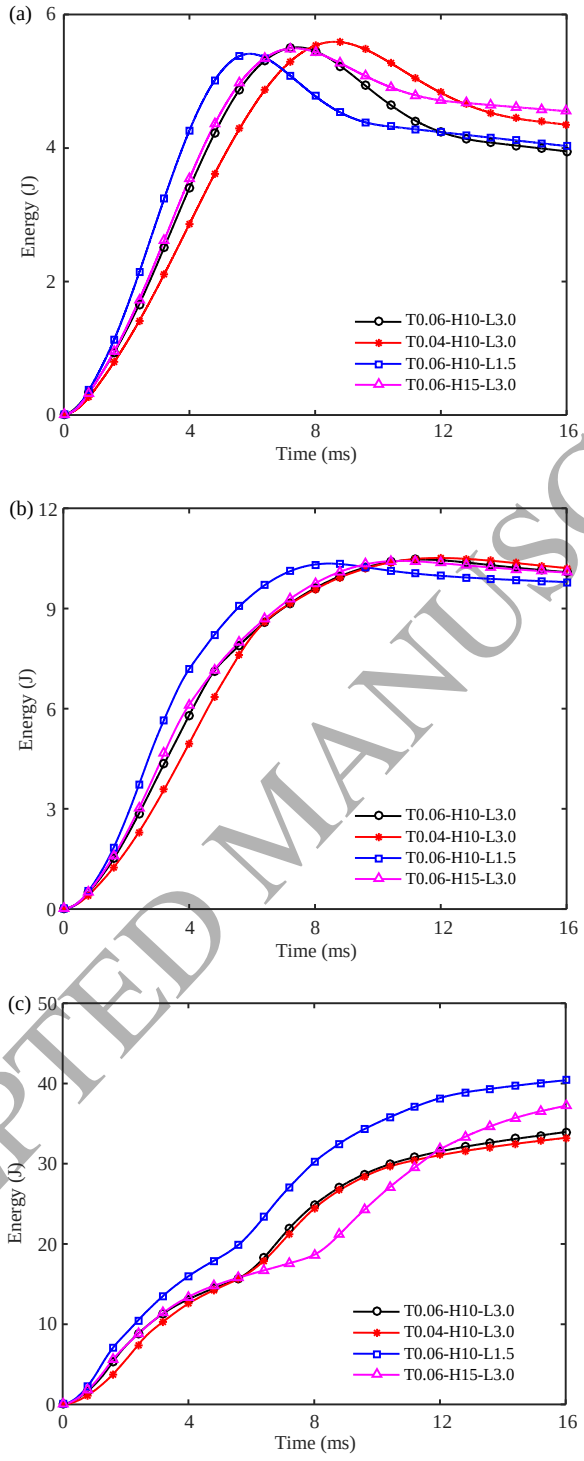

Fig. 9. Absorbed energy-time curves of specimens under various impact energy levels: (a) 5 J; (b) 10 J; (c) 40 J.

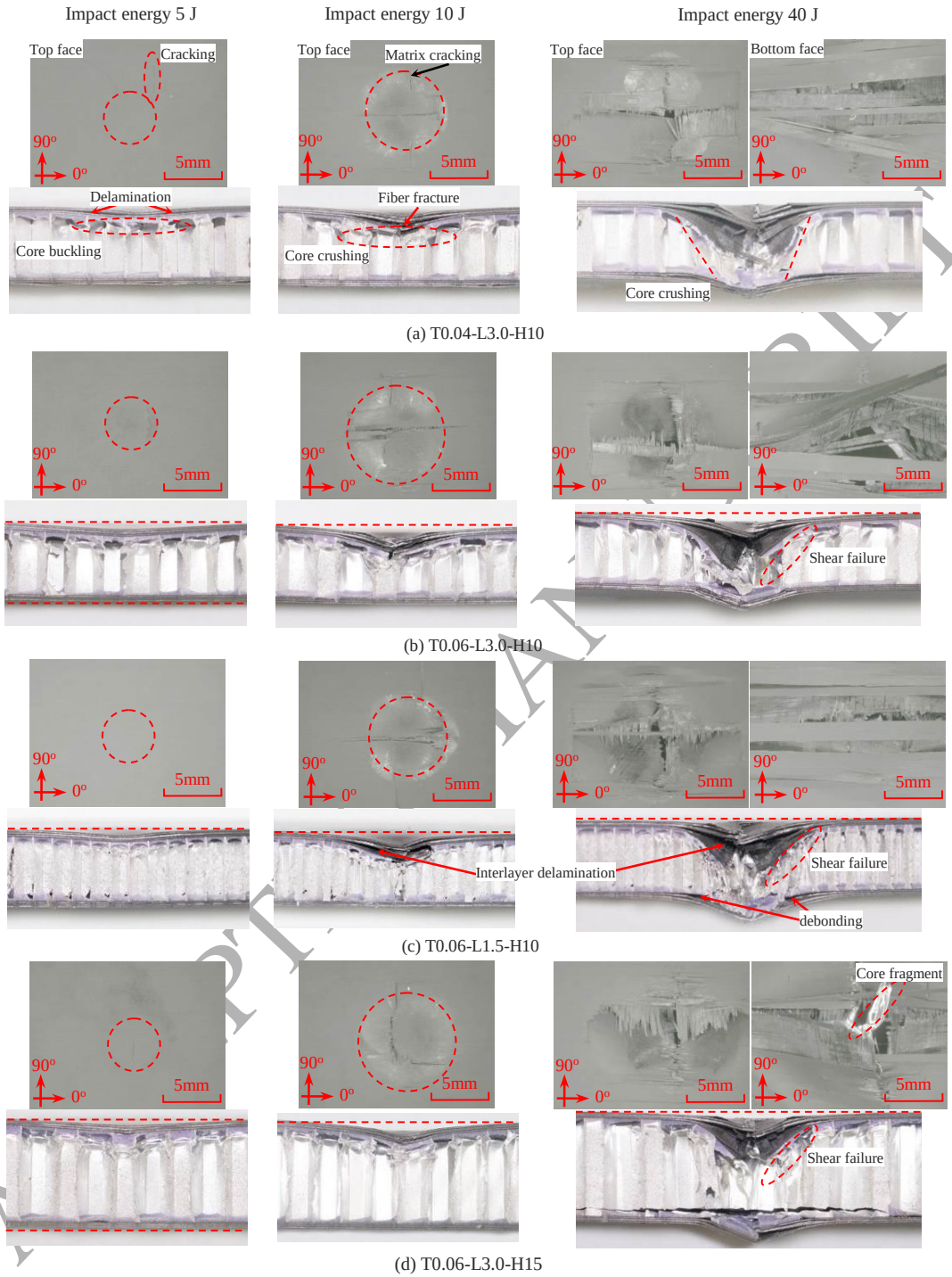

Fig. 10. Damage pattern of the specimens under different incident impact energies.

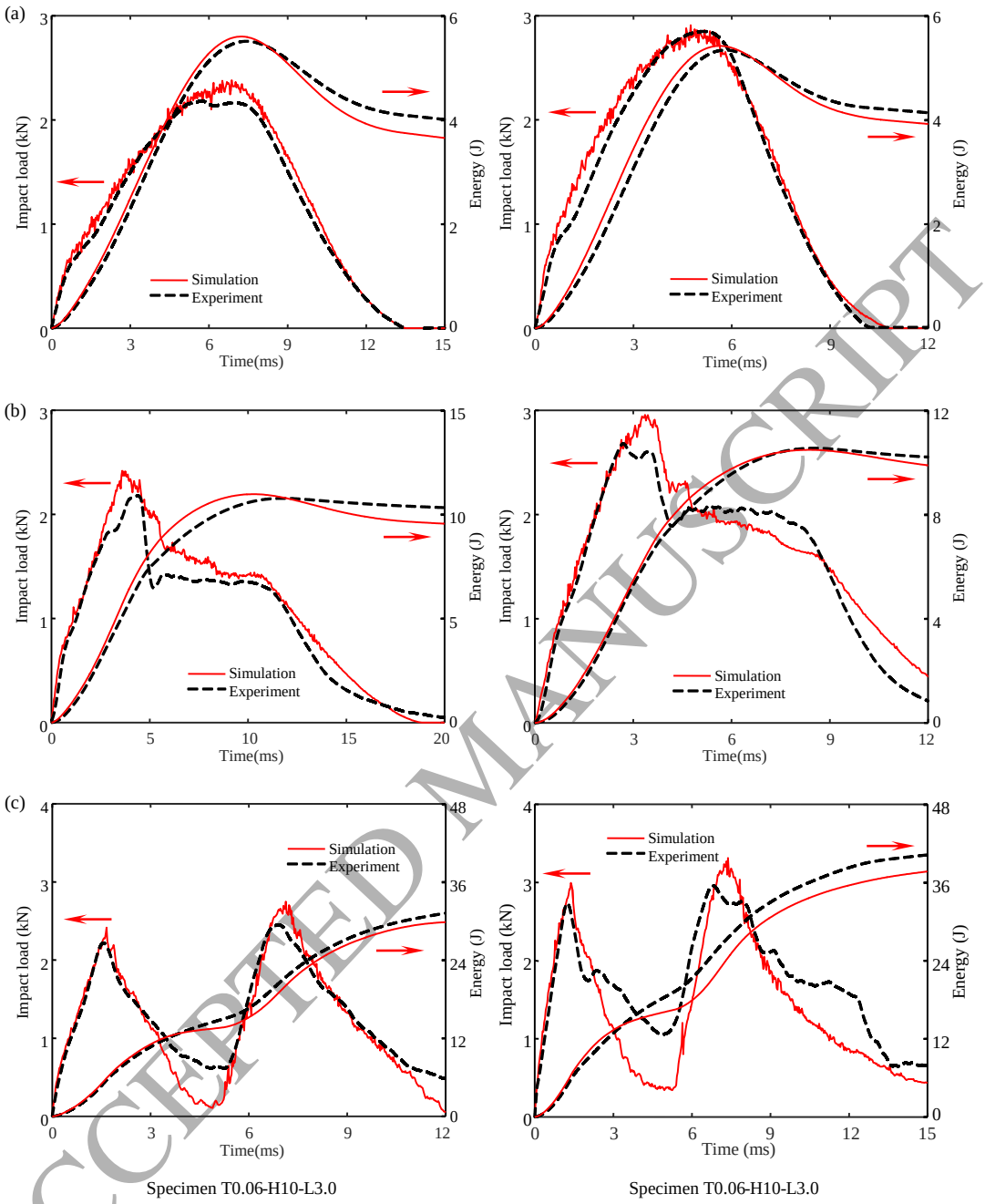

Fig. 11. Comparison of impact load and absorbed energy curves for specimens T0.06-H10-L3.0 and T0.06-H10-L1.5 under various impact energy levels: (a) 5 J; (b) 10 J; (c) 40 J.

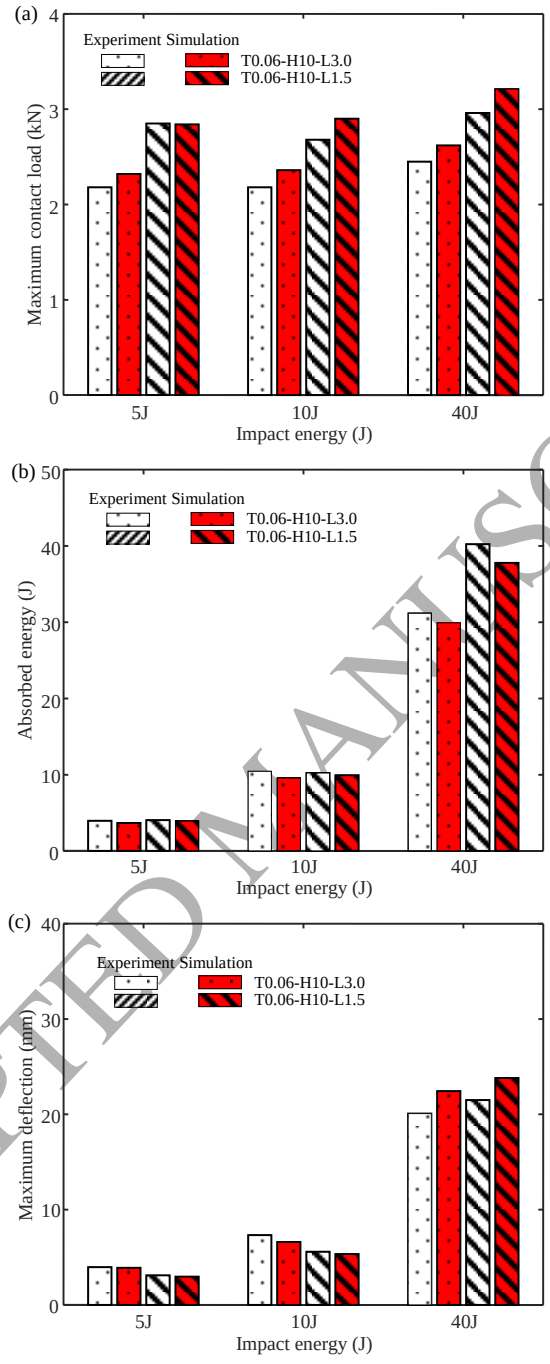

Fig. 12. Comparison of key characteristics for specimens T0.06-H10-L3.0 and T0.06-H10-L1.5 under various impact energy levels: (a) maximum contact force; (b) absorbed energy; and (c) maximum deflection.

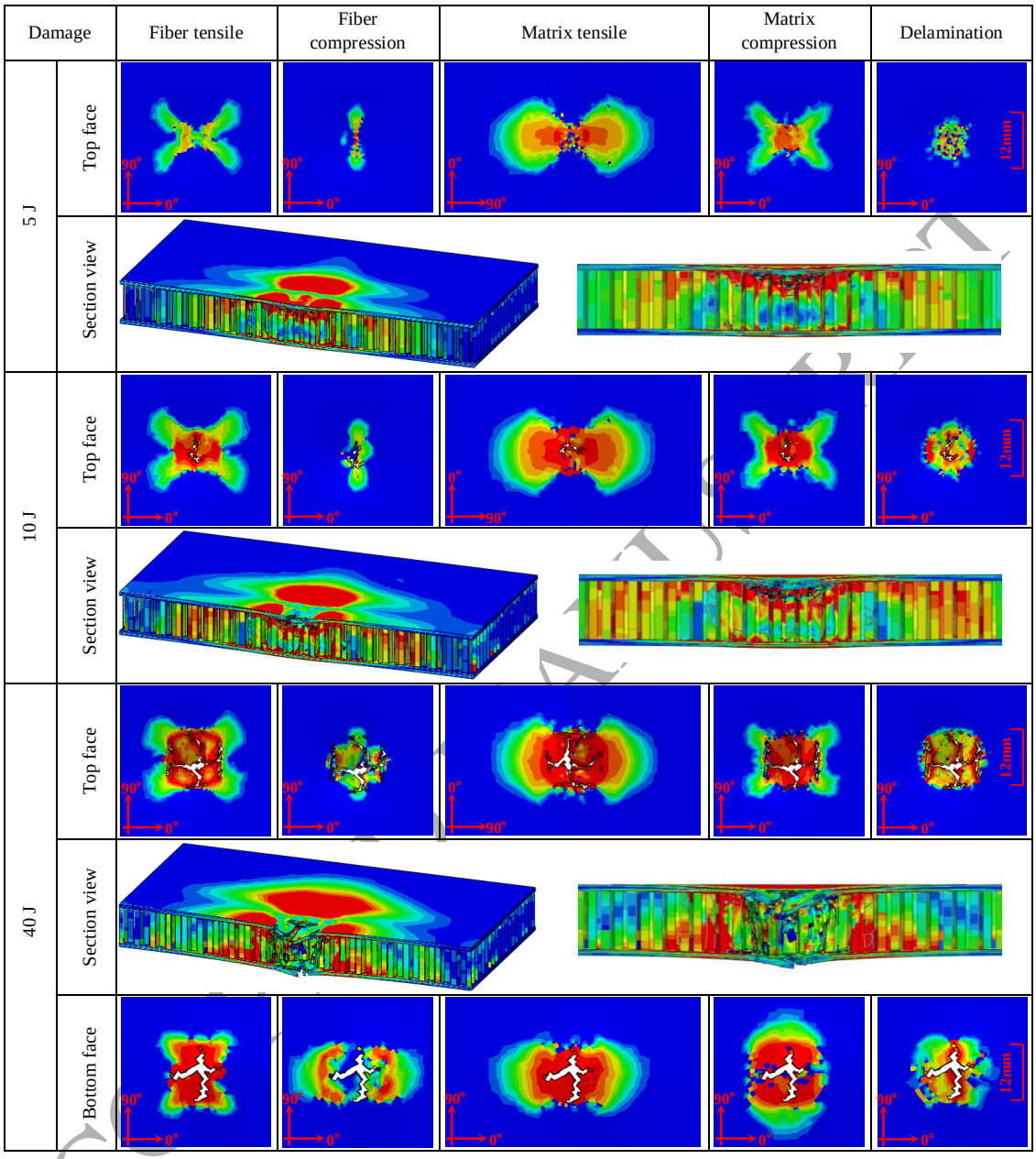

Fig. 13. Predicted impact damage of specimen T0.06-H10-L1.5 under various impact energy levels.

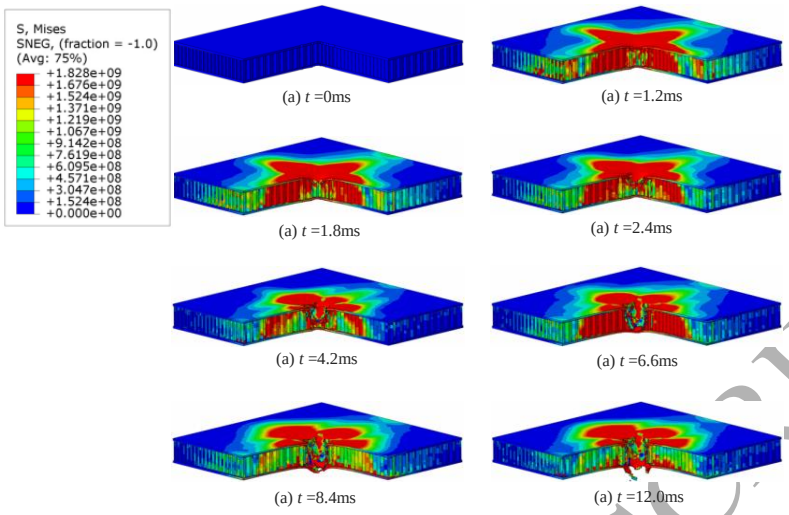

Fig. 14. Deformation process of specimen T0.06-H10-L1.5 at different contact time.

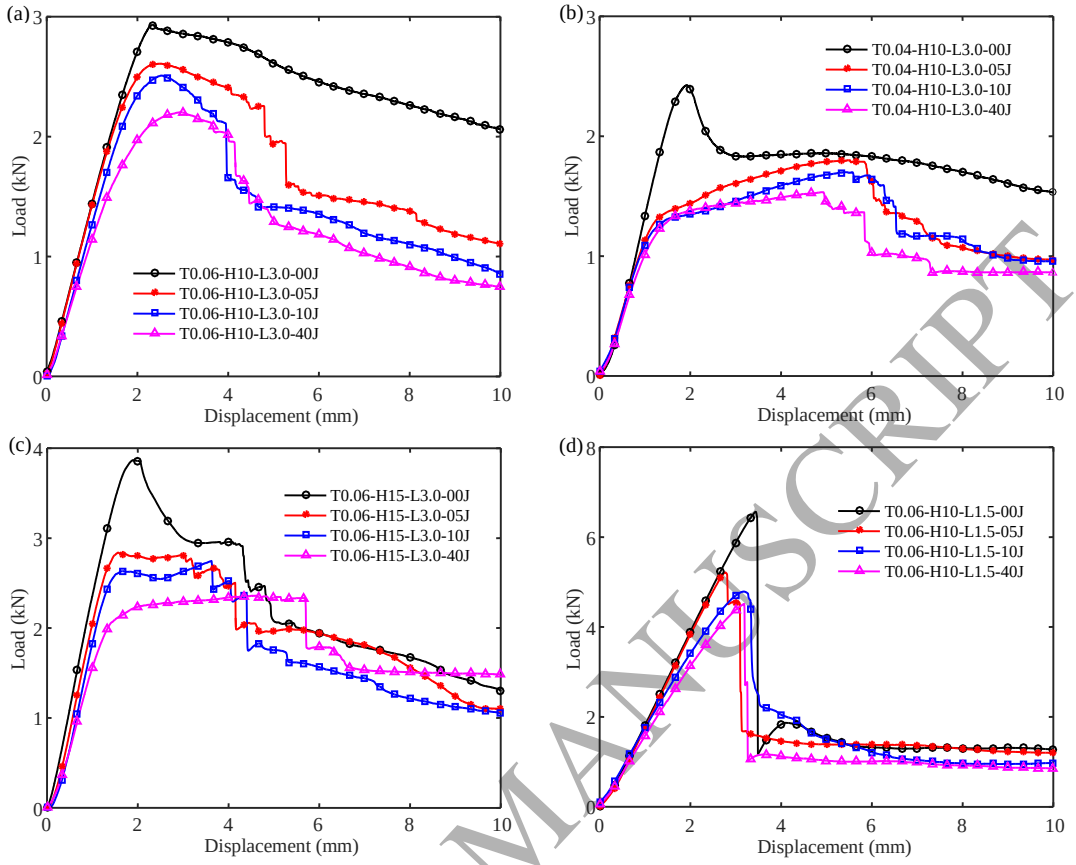

Fig. 15. Force-displacement curves of specimens with different structural configurations under various impact energy levels: (a) specimen T0.06-H10-L3.0; (b) specimen T0.04-H10-L3.0; (c) specimen T0.06-H15-L3.0; (a) specimen T0.06-H10-L1.5.

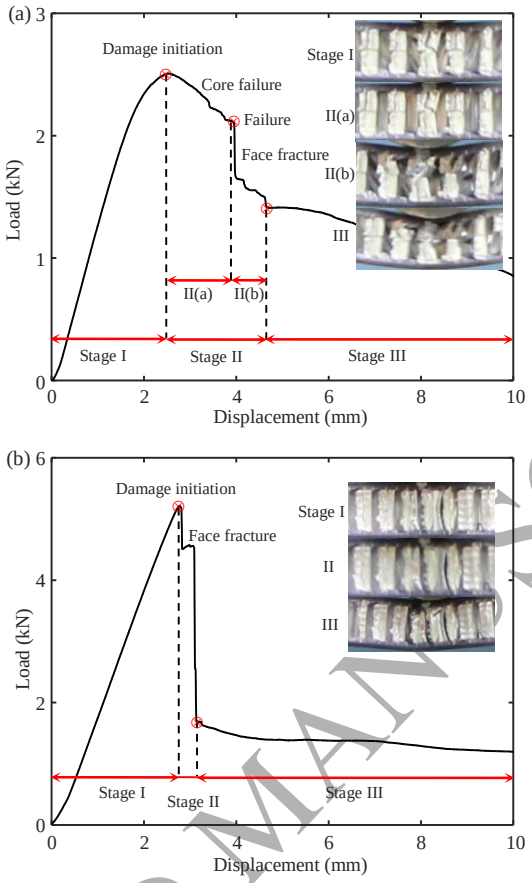

Fig. 16. Two typical load curve and damage process: (a) core failure; (b) face sheet failure.

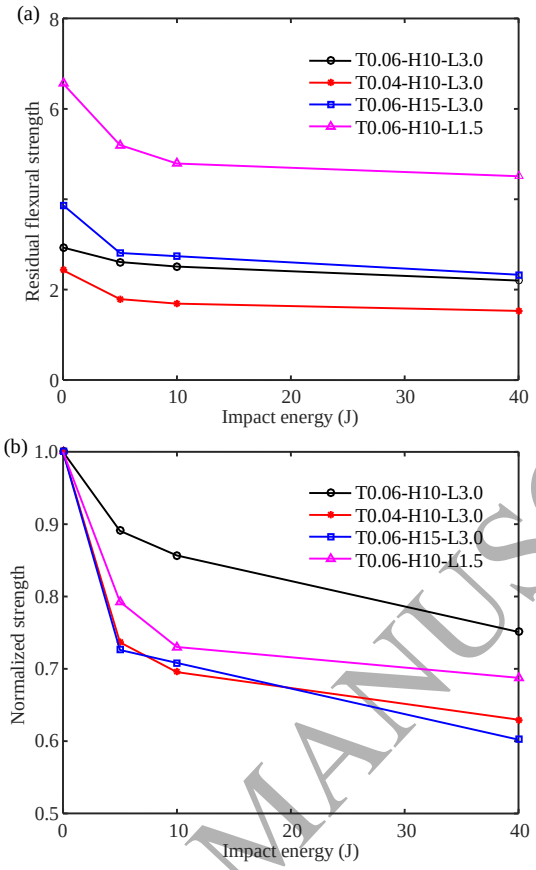

Fig. 17. Residual flexural strengths and normalized residual flexural strengths of specimens under various impact energy levels.

(a) Specimen T0.06-H10-L3.0

(b) Specimen T0.04-H10-L3.0

(c) Specimen T0.06-H15-L3.0

(d) Specimen T0.06-H10-L1.5

Fig. 18. Deformation and failure mode of non-impacted specimens.

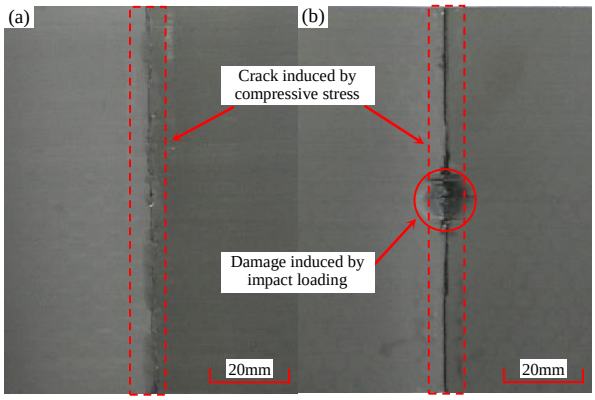

Fig. 19. Damage morphology of specimen T0.06-H10-L3.0 after impact: (a) non-impacted specimen; (b) specimen impacted under 10 J impact energy.

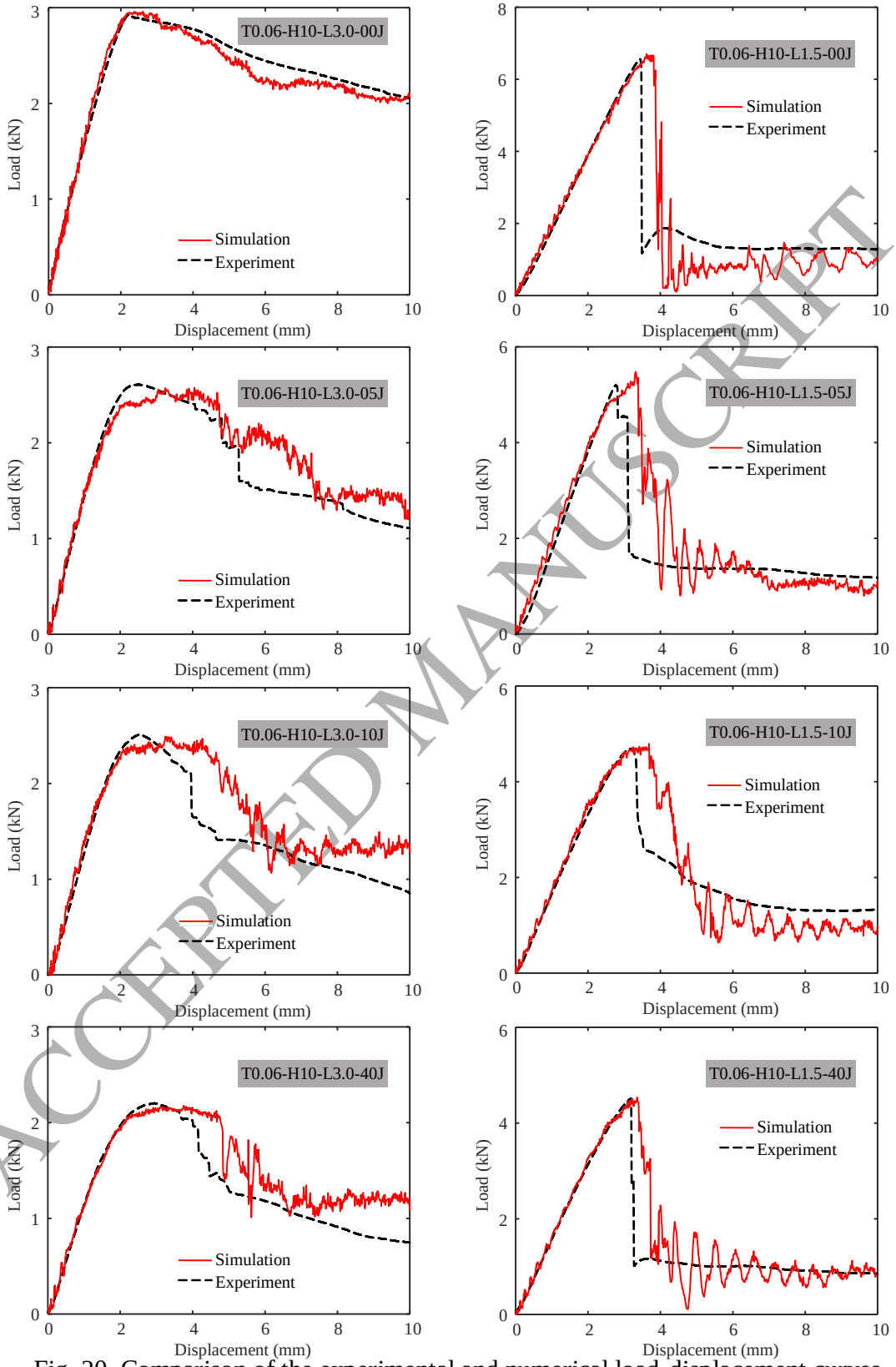

Fig. 20. Comparison of the experimental and numerical load-displacement curves.

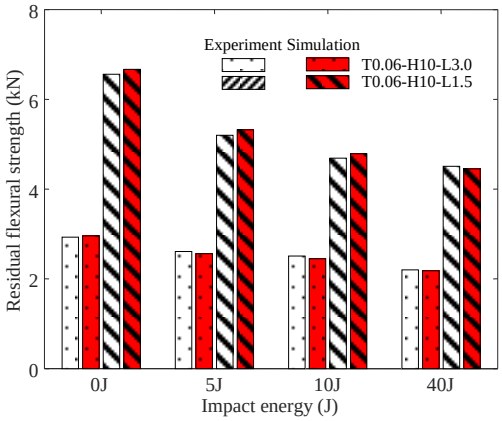

Fig. 21. Comparison of residual flexural strength between numerical and experimental results.

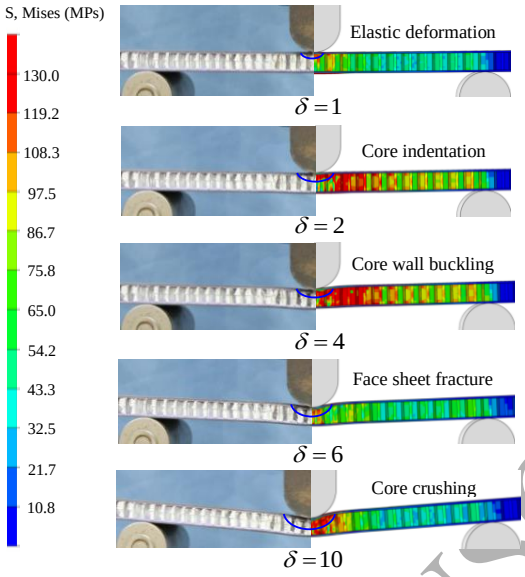

Fig. 22. Numerical simulation and captured images of crushing process for specimen T0.06-H10-L3.0 in various stages.

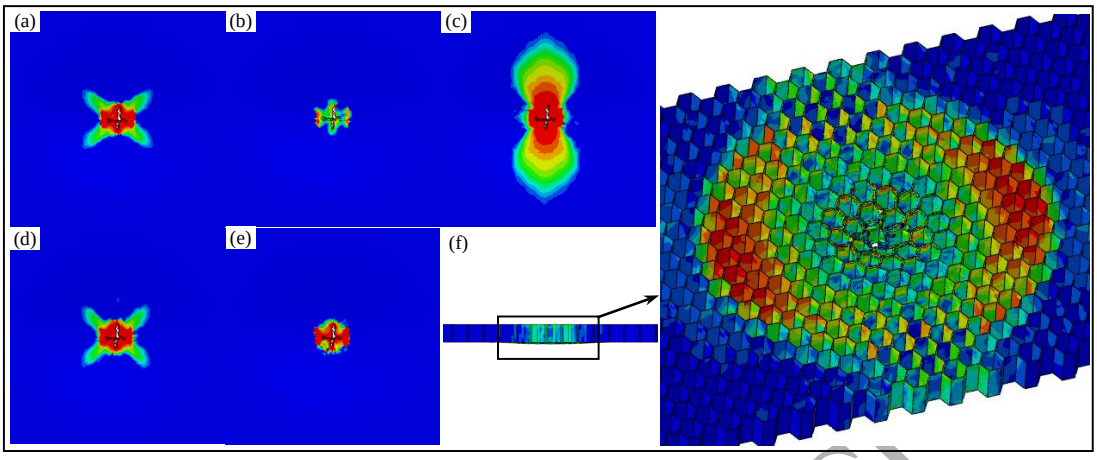

Damage patterns after impact

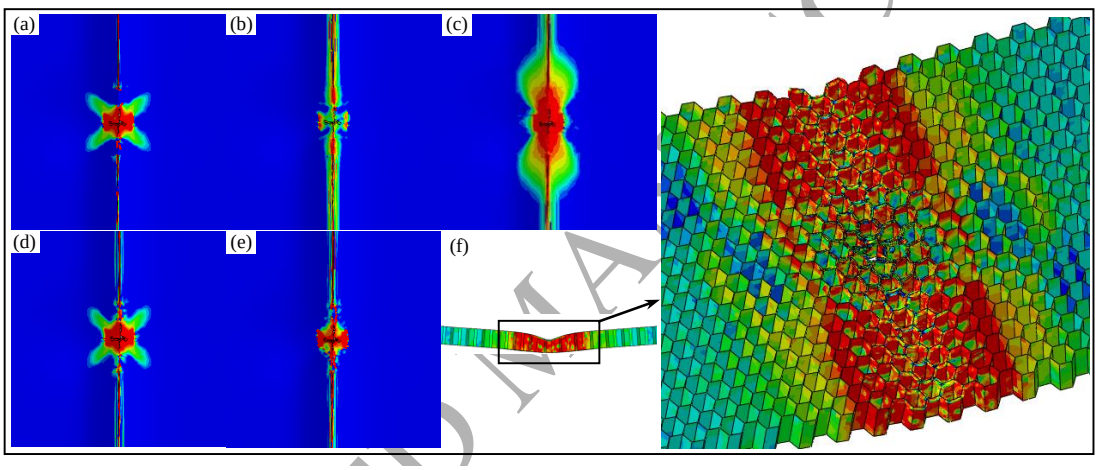

Damage patterns after bending for the impacted specimen

Fig. 23. Comparison of predicted failure modes for the top face sheet and honeycomb core (specimen T0.06-H10-L3.0): (a) fiber tensile failure; (b) fiber compressive failure; (c) matrix tensile failure; (d) matrix compressive failure; (e) delamination failure; and (f) core failure.

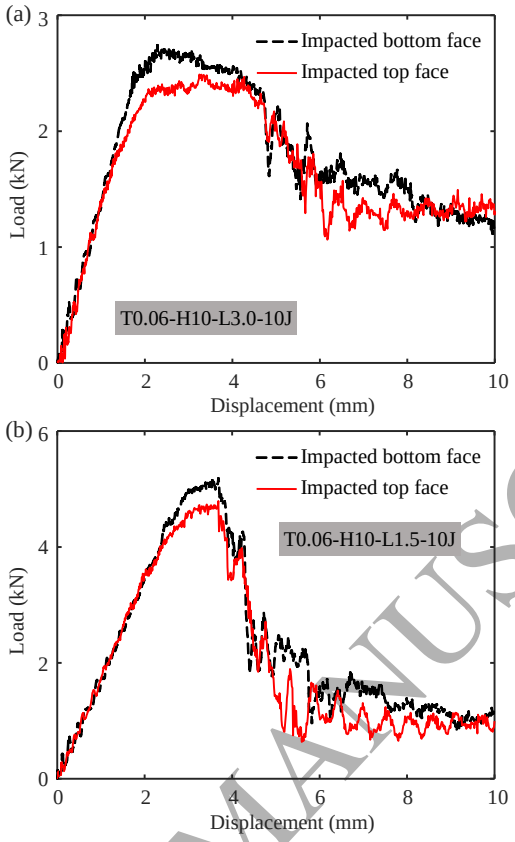

Fig. 24. Comparison of load-displacement curves for specimen applied loading on the impacted surface and its apposite surface.

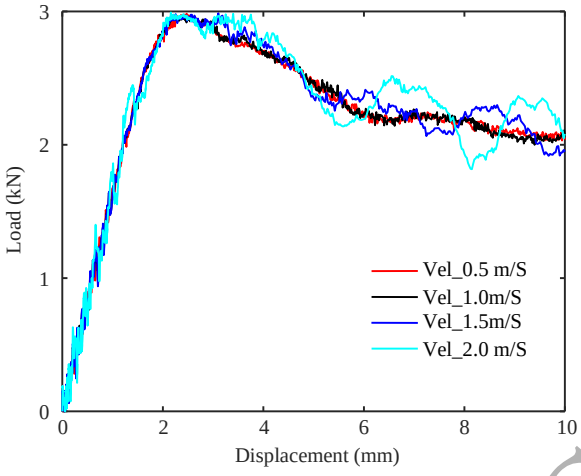

Fig. A.1. Comparison of different loading speed for bending simulation.

Graphical Abstract